

Thermal and Mechanical Vibration Response of Auxetic Core Sandwich Smart Nanoplate

Mehmet Akif Koç, İsmail Esen, and Mustafa Eroğlu*

This study explores a new nanoplate design's thermal and mechanical properties, including an auxetic core with a negative Poisson ratio. The core is between face plates made of barium–cobalt, which possess magnetoelastoelectric properties. The analysis centers on the parameters θ , β_1 , and β_2 to clarify their influence on the nanoplate's performance. The evaluations of the nanoplate's thermal, electrical, and magnetic properties showcase its remarkable versatility and sensitivity. Incorporating magnetoelastoelectric face plates improves the multifunctionality of the nanoplate, making it a highly promising option for use in smart technologies. The findings offer valuable insights into the distinctive features of auxetic core structures, significantly enhancing the comprehension of these materials. This research emphasizes the potential for creating groundbreaking applications in fields like aerospace engineering and advanced electronics, where versatile and adaptable materials play a vital role. This study contributes to the broader knowledge of auxetic materials and their practical implementation in cutting-edge technological solutions by exploring the interplay between thermal, mechanical, and magnetoelastoelectric properties.

applications. This is because they have a high flexural stiffness-to-weight ratio, which is better than traditional materials. Sandwich composites have become the preferred option in many sectors with their distinctive blend of low weight and strong flexural stiffness. They offer excellent performance and superior strength in numerous applications.^[1,2] The study^[3] increases bonding with vacuum-assisted material extrusion to improve the mechanical properties of the flax fiber sandwich composite. Composites with 2 and 25.4 mm skin/core thicknesses showed 36.6%, 27.2%, 12.3%, and 9.5% strengths and stiffness and 47.3% and 101.5% loading cycles in three-point bending and short-beam shear loads. Sandwich composites are advanced technology, with two thin, robust shells around a lightweight core. Protective skins have in-plane strength and stiffness and substantial out-of-plane strength to safeguard the core structure. Sandwich composites' complex structure gives them a mechanical edge in applications that require in-plane and out-of-plane structural stability. In sandwich composites, core materials improve the bending strength of the plate^[4,5] and buckling performance,^[6,7] while simultaneously causing a slight increase in the overall weight of the composite. Developing innovative core structures and geometries is crucial in strengthening the material's resistance to impact load applications.^[8,9] Sandwich composites with polyvinyl chloride (PVC) cores and glass–fiber-reinforced epoxy-laminated composites are compared for maritime transport reel mechanical response. In three-point bend tests, a composite sandwich with a PVC core absorbs 39% more energy than a laminate composite. Experimental and numerical simulations match, proving model fidelity.^[10] The advancement of core structures and geometries is the primary focus of ongoing attempts to raise the impact resistance of materials. Examples of core structures frequently encountered are foams, honeycomb structures in cells,^[11] and cellular architectures with lattice topology.^[12] Sandwich composites with auxetic cores, which possess a negative Poisson's ratio, have attracted considerable interest due to their outstanding properties, especially their impressive lightness.

1. Introduction

Sandwich composites are commonly used in applications that need low weight, such as aircraft components, aerospace technologies, automotive structures, sports equipment, and marine


applications that require in-plane and out-of-plane structural stability. In sandwich composites, core materials improve the bending strength of the plate^[4,5] and buckling performance,^[6,7] while simultaneously causing a slight increase in the overall weight of the composite. Developing innovative core structures and geometries is crucial in strengthening the material's resistance to impact load applications.^[8,9] Sandwich composites with polyvinyl chloride (PVC) cores and glass–fiber-reinforced epoxy-laminated composites are compared for maritime transport reel mechanical response. In three-point bend tests, a composite sandwich with a PVC core absorbs 39% more energy than a laminate composite. Experimental and numerical simulations match, proving model fidelity.^[10] The advancement of core structures and geometries is the primary focus of ongoing attempts to raise the impact resistance of materials. Examples of core structures frequently encountered are foams, honeycomb structures in cells,^[11] and cellular architectures with lattice topology.^[12] Sandwich composites with auxetic cores, which possess a negative Poisson's ratio, have attracted considerable interest due to their outstanding properties, especially their impressive lightness.

Auxetic core structures, such as beams and plates, are essential in engineering due to their distinctive negative Poisson's ratio, which confers excellent mechanical properties. These properties make them indispensable in fields such as aerospace and automotive design, providing lightweight and versatile solutions

M. A. Koç
Mechatronics Engineering Department
Sakarya Applied Sciences University
54187 Sakarya, Turkey

İ. Esen
Mechanical Engineering Department
Karabük University
78050 Karabük, Turkey

M. Eroğlu
Mechanical Engineering Department
Sakarya University
54187 Sakarya, Turkey
E-mail: mustafaeroglu@sakarya.edu.tr

 The ORCID identification number(s) for the author(s) of this article can be found under <https://doi.org/10.1002/adem.202400797>.

© 2024 The Author(s). Advanced Engineering Materials published by Wiley-VCH GmbH. This is an open access article under the terms of the Creative Commons Attribution-NonCommercial-NoDerivs License, which permits use and distribution in any medium, provided the original work is properly cited, the use is non-commercial and no modifications or adaptations are made.

DOI: 10.1002/adem.202400797

to improve safety and efficiency in engineering. The study introduces a sandwich beam with enhanced auxetic core (SCH SWB) to overcome auxetic structures' low stiffness and strength. SCH SWB tests and simulations show improved energy absorption and bending resistance.^[2] The study^[13] examines the nonlinear vibration of a sandwich panel with functionally graded (FG) material and a double-U auxetic core under heat conduction. It confirms findings, examines parameter impacts, and highlights aircraft component design significance. Sandwich beams with auxetic honeycomb cores are studied for nonlinear thermally generated vibration.^[14] The research^[15] uses higher-order shear deformation theory to study the nonlinear behavior of a honeycomb core and graphene platelet-reinforced microcomposite sandwich plate. Findings show that core thickness ratio, inclined angle, and thickness to inclined length significantly affect nonlinear frequencies and deflection response, guiding aircraft part development. Reduced honeycomb tilt reduces vibrations, and geometric nonlinearity depends on thermal shock shape. Thermal buckling is a crucial component, and the study offers design insights to reduce sandwich structure vibrations. The study^[16] examines the nonlinear vibration of a sandwich plate with an auxetic honeycomb core and a carbon nanotube-reinforced composite (CNTRC) front layer on a viscous elastic base. Considering high strength-to-weight ratios and energy absorption, findings inform aeronautical and automotive design. A piezoelectric auxetic honeycomb sandwich plate on an elastic substrate is examined for its nonlinear dynamics and free vibration.^[17] It examines how material, geometry, and substrate coefficients affect frequency and nonlinear characteristics in open and closed circuits under varied boundary conditions. The study^[18] examines the dynamic behavior of plates made of FG-CNTRC materials with a negative Poisson ratio. The explicit solutions provide a range of effective Poisson's ratio (EPR) values, with EPR ranging from 0.311 to -0.63 . Numerical simulations analyze the dynamic behavior of a system, considering aspects such as the distribution of functional gradients and thermal stress. A recent study^[19] delves into auxetic materials' thermal and mechanical properties, showcasing their potential in advanced engineering applications. In recent research,^[20] the analysis of sandwich plates with auxetic cores has shown remarkable multifunctional advancements, making them highly compatible with smart technologies. Their development highlights the versatility of multifunctional auxetic nanocomposites in smart applications, demonstrating their potential for broader use in industry.^[21]

Magneto-electroelastic (MEE) materials, including piezoelectric and piezomagnetic phases, are a notable class of intelligent materials. These materials possess piezoelectric and piezomagnetic characteristics and display strong coupling effects between mechanical, electric, and magnetic states. MEE materials have the potential to transform energy between different forms, making them useful in a wide range of industries, including aerospace, sensors, civil engineering, medical equipment, and automotive technology.^[22] Recently, there has been a significant increase in research dedicated to examining the reaction and durability of MEE structures. Zhang et al. proposed a new model for Timoshenko beams that are both transversely isotropic and MEE. They used a variational formulation based on Hamilton's principle.^[23] In their study, Zur et al.^[24] examined the behavior of

FG nanoplates with MEE coupling, specifically focusing on the effects of free vibration and buckling reactions. The researchers utilized a nonlocal modified sinusoidal shear deformation plate theory that accounts for the influence of thickness stretching. The study^[25] studies the nonlinear dynamic response of an aerospace and industry-critical FG MEE nanobeam. It considers early geometric defects, validates the model, and emphasizes MEE coupling for advanced device design. The study^[26] examines the low-velocity behavior of MEE plates in aviation and spaceflight using electric, magnetic, and thermal fields. The lowest BaTiO₃ volume fraction MEE plates had lower displacement, shorter contact duration, and higher contact force. Size effects are considered when analyzing MEE nanobeam bending on a Winkler–Pasternak foundation.^[27] Nonlinear deflection is solved by the Galerkin method and nonlocal modified couple stress theory. We explore key parameter impacts. In recent years, there has been considerable interest in the examination of MEE face layers. In their study,^[28] the analysis of a vibration energy harvester that utilized an auxetic core and MEE facings is examined. Their research provided insights into the possible uses of MEE materials in energy harvesting technologies. In addition,^[29] how the arrangement and composition of foam in sandwich nanoplates with MEE face layers affect their thermomechanical vibration behavior is investigated. This study offers vital knowledge on the dynamic properties of MEE materials in composite structures.

The engineering relevance of sandwich auxetic nanoplates is their distinctive structural qualities, which offer a foundation for new materials with enhanced mechanical capabilities. The unique shape of these nanoplates presents novel possibilities for a wide range of technical applications, including aerospace and biomedical engineering, due to their capacity for enhanced flexibility, strength, and customizable capabilities.^[30–32] The study^[33] examines auxetic honeycomb-cored FG sandwich nanobeam static buckling and bending. Using third-order shear deformation theory, the model simulates mechanical behavior and examines how parameters affect critical buckling load and maximum deflection. The study^[34] examines blast-loaded double-layer auxetic FG porous sandwich plate static bending and vibration. The structure has two auxetic effective Poisson's ratio values, with EPR FGM sandwich layers. Results may apply to explosive-loaded constructions. The study^[35] investigates sandwich plate-free vibration and buckling with auxetic honeycomb core and polymer/GNP/fiber face sheets. The sinusoidal shear deformation theory examines how core geometry, GNP/fiber fractions, and thickness affect critical buckling loads and natural frequencies. As honeycomb core thickness grows, critical buckling loads decrease, and natural frequencies rise and fall.

This article introduces a new examination of the thermal and mechanical reactions of a nanoplate that has an auxetic core, which is improved by MEE face plates. This research reveals the exceptional adaptability and responsiveness of the nanoplate by examining factors such as θ , β_1 , and β_2 . It provides insights into the thermal, electrical, and magnetic characteristics of the nanoplate. The addition of MEE face plates enhances the versatility of the nanoplate, making it a highly promising option for smart technology. The combination of these components not only enhances the understanding of auxetic core structures but also opens up opportunities for innovative applications in

aerospace engineering and advanced electronics. This study stands out by examining the complex relationship between the fundamental structure, properties of the face plate, and performance measures. As a result, it makes a substantial contribution to the ongoing effort to develop revolutionary materials with exceptional mechanical capabilities and multifunctionality.

2. Mathematical Modeling

The mathematical model used in this study is based on Hamilton's technique, which is applied to develop the equations of motion for MEE face plates with FG nanoplates. This allows for the analysis of the nanoplate's dynamic response and its sensitivity to thermal stresses, MEE coupling, externally supplied electric and magnetic fields, nonlocal properties, porosity volume fraction, and variations in porosity across its thickness. The model takes into consideration the various attributes of the constituent materials of the nanoplate, as well as their influence on the thermomechanical behavior of the nanoplate.

2.1. Effective Material Properties of Porous Laminated Nanoplate

Consider a three-layer rectangular plate, given in **Figure 1**, placed on a Cartesian coordinate system (x, y, z) having a (length) and b (width) lengths in x and y directions. Thus, the total thickness of the plate H_t is given by the summation of the core h and surface h_s layers as in the $H_t = h + 2h_s$ equation. Ω denotes the plate's middle plane for the undeformed case. Thus, the tensor $\Omega x = (-h_s - h/2, h/2 + h_s)$ stands for the plate's total domain border placed between the bottom ($z = -h_s - h/2$) and the top ($z = h_s + h/2$) surfaces and the edge. The curved surface Γ , defined by the tensor $\Gamma x(-h_s - h/2, h/2 + h_s)$, has an outward normal $\hat{n} = n_x \hat{e}_x + n_y \hat{e}_y$ with the n_x and n_y as the unit normal's direction cosines. The face plate consists of several layers, each with its own designated coordinates. The lower face plate is represented by h_1 and h_2 , the rim plate below is represented by h_3 ,

the auxetic core plate is represented by h_4 , the rim plate above is represented by h_5 , and the upper face plate is represented by h_6 .

To accurately forecast the behavior of the building, it is deemed necessary to consider the effects of temperature. Hence, the temperature-dependent properties of the material include the elastic modulus E_{ef} , the effective Poisson's ratio ν_{ef} , the conductivity coefficients ψ_{ef} , and thermal expansion κ_{ef} . A nonlinear function of temperature can describe these properties.^[36,37]

$$P = P_0(P_{-1}T^{-1} + 1 + P_1T + P_2T^2 + P_3T^3) \quad (1)$$

In this context, P symbolizes any temperature-dependent constituent, while P_0 refers to each substance. The table displays the P_{-1} , P_1 , P_2 , and P_3 values for different orders ($-1, 0, 1, 2,$ and 3) of the temperature T , as presented in **Table 1** and **2**. The mass density $\rho(z)$ is a function solely dependent on z and is significantly influenced by variations in temperature, as determined by the effective material properties.

2.2. Auxetic Core

The sandwich plate design includes an auxetic material with a negative Poisson's ratio as its core layer, demonstrating improved mechanical properties when subjected to different loads and strains. The aluminum auxetic core exhibits expansion and contraction in response to tensile and compressive loads. The geometrical parameters of the auxetic unit cell, such as the inclined angle (θ) , rib thickness (t) , length of the vertical wall (d) , and length of the inclined wall (l) , are depicted in **Figure 1**. The elastic characteristics and mass density of the auxetic core are calculated by applying the equations^[38] that describe the properties of aluminum.

$$E_{11}^c = E_{Al} \left[\frac{(\beta_1 - \sin(\theta)\beta_3^3)}{[(\beta_1 \sec^2(\theta) + \tan^2(\theta))\beta_3^2 + 1]\cos^3(\theta)} \right] \quad (2)$$

$$E_{22}^c = E_{Al} \left[\frac{\beta_3^3}{(\beta_3^2 + \tan^2(\theta) + 1)(\cos(\theta)\beta_1 - \cos(\theta)\sin(\theta))} \right] \quad (3)$$

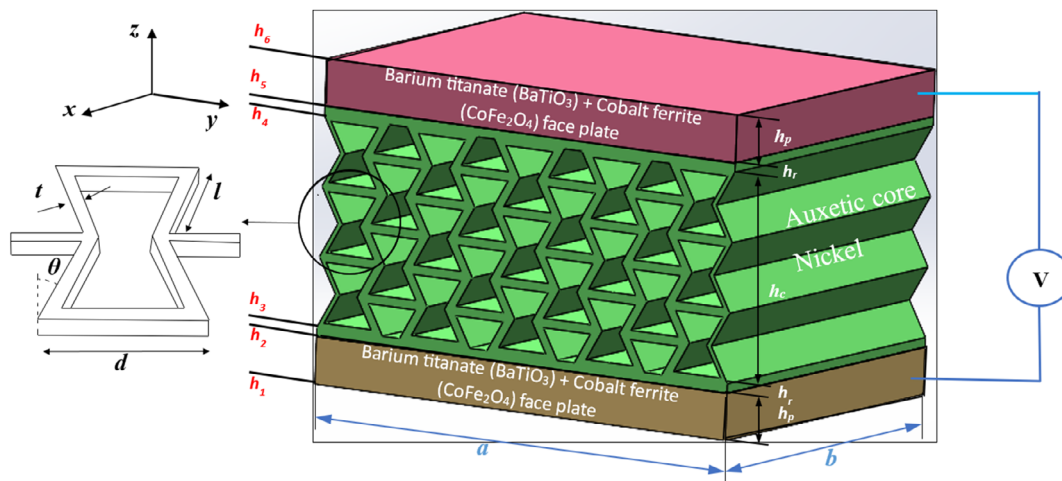


Figure 1. A higher order nanoplate with auxetic core structure and face layers under electric and thermal effects.

Table 1. Temperature-dependent coefficients for the properties of CoFe₂O₄ and BaTiO₃.

Material	Property	P_{-1}	P_0	P_1	P_2	P_3
CoFe ₂ O ₄	C_{11} [Pa]	0	298.87e9	-1.552e-4	6.125e-9	-9.0e-11
	C_{55} [Pa]	0	47.33e9	-1.552e-4	6.125e-9	-9.0e-11
	ν	0	0.3	0	0	0
	α [1 K ⁻¹]	0	7.5e-6	-3.01e-4	4.02e-6	-1.01e-09
	κ [W mK ⁻¹]	0	4.7030	-0.0011	1.6612e-06	-9.9670e-10
	ρ [kg m ⁻³]	0	5300	0	0	0
BaTiO ₃	C_{11} [Pa]	0	174e9	-1.552e-4	6.125e-9	-9.0e-11
	C_{55} [Pa]	0	44.93e9	-1.552e-4	6.125e-9	-9.0e-11
	ν	0	0.30	0	0	0
	α [1 K ⁻¹]	0	10e-6	-3.0e-4	4.0e-6	-1.0e-09
	κ [W mK ⁻¹]	0	3.7624	-8.50521e-4	1.32894e-06	-7.97363e-0
	ρ [kg m ⁻³]	0	5800	0	0	0

Table 2. The magnetic, piezo, electro, and thermal properties of CoFe₂O₄ and BaTiO₃.

		CoFe ₂ O ₄	BaTiO ₃
C_{11}	[GPa]	286	166
C_{22}		286	166
C_{33}		269.5	162
C_{12}		173	77
C_{13}		170.5	78
C_{23}		170.5	78
C_{44}		45.3	43
C_{55}		45.3	43
C_{66}		56.5	44.5
e_{31}	[C m ⁻²]	0	-4.4
e_{32}		0	-4.4
e_{33}		0	18.6
q_{31}	[N A ⁻¹ m ⁻¹]	580.3	0
q_{32}		580.3	0
q_{33}		699.7	0
ξ_{11}	[10 ⁻⁹ C ² N ⁻¹ m ⁻²]	0.08	11.2
ξ_{22}		0.08	11.2
ξ_{33}		0.093	12.6
$\zeta_{11} = \zeta_{22} = \zeta_{33}$	[s m ⁻¹]	0	0
χ_{11}	[10 ⁻⁶ N s ² C ⁻¹]	-590	5
χ_{22}		-590	5
χ_{33}		157	10
$p_{11} = p_{22}$	[10 ⁻⁷ C m ⁻² K ⁻¹]	0	0
p_{33}		0	-11.4
$\lambda_{11} = \lambda_{11}$	[10 ⁻⁵ Wb m ⁻² K ⁻¹]	0	0
λ_{33}		-36.2	0
$\alpha 1 = \alpha 1$	[10 ⁻⁶ K ⁻¹]	10	15.8
ρ	[kg m ⁻³]	5800	5300

$$G_{12}^c = E_{Al} \left[\frac{\beta_3^3}{(2\beta_1^2 + \beta_1) \cos(\theta)} \right] \quad (4)$$

$$G_{13}^c = G_{Al} \left[\frac{2\sin^2(\theta) + \beta_1}{2(\eta_1 - \sin(\theta)) \cos(\theta)} \right] \quad (5)$$

$$\rho^c = \rho_{Al} \left[\frac{(2 + \beta_1)\beta_3}{2(\beta_1 - \sin(\theta)) \cos(\theta)} \right] \quad (6)$$

The parameters $\beta_1 = d/l$ and $\beta_3 = t/l$ are defined, and the Poisson's ratio can be directly derived from the geometrical characteristics of the auxetic unit cells, as outlined in another study.^[38]

$$v_{12}^c = \frac{(\sin(\theta) - \beta_1)(\sin(\theta))(1 - \beta_3^2)}{\cos^2(\theta)[\beta_3^2(\beta_1 \sec^2(\theta) + \tan^2(\theta)) + 1]} \quad (7)$$

$$v_{21}^c = \frac{(\beta_3^2 - 1) \sin(\theta)}{(\beta_1 - \sin(\theta))(\beta_3^2 + \tan^2(\theta))} \quad (8)$$

2.3. The Nonlinear Temperature Increment

This section presents the applicable equations for uniform temperature rise (UTR), linear temperature rise (LTR), and nonlinear temperature rise (NLTR) across the whole thickness of the nanorod. The entire structure of a FGM nanobeam, initially at a temperature of $T_0 = 300$ K, is uniformly raised to its final temperature T . This is achieved by applying the equation for stress-free conditions with UTR.

$$\Delta T = T - T_0 \quad (9)$$

The temperature of a plane in the z-direction can be determined using Equation (56), which takes into account the temperatures of the bottom and top surfaces (T_b and T_t) and assumes a LTR from T_b to T_t throughout the thickness.^[39]

$$T(z) = T_b + (T_t - T_b) \left(\frac{h + 2z}{2h} \right) \quad (10)$$

We can solve the steady-state 1D heat transfer equation shown below to estimate the temperatures of the top (T_t) and bottom (T_b) surfaces of the nanobeam when NLTRs rise across its thickness. This equation takes into account the known temperature boundary conditions.^[40]

$$-\frac{d}{dz} \left(\kappa(z) \frac{dT}{dz} \right) = 0, \quad T\left(\frac{h}{2}\right) = T_t, \quad T\left(-\frac{h}{2}\right) = T_b \quad (11a)$$

Consequently, the temperature at any z extending along the thickness for a specified boundary condition is

$$T(z) = T_b + \frac{(T_t - T_b)}{\int_{-\frac{h}{2}}^{\frac{h}{2}} \frac{1}{\psi(z)} dz} \int_{-\frac{h}{2}}^z \psi(z) dz \quad (11b)$$

2.4. Review of the Nonlocal Strain Gradient Theory (NSGT) for the MEE Material

The stress at one point in a continuous body is thought to be dependent on all other points in the body according to Eringen's research.^[41] Based on this theory, the magnitude of impacts at both the material and nonlocal scales determines the structure's stiffness. This structure behaves more smoothly than classical forms, depending on the strength of the nonlocal impact. The strain gradient hypothesis, on the other hand, increases structural stiffness to purely account for material scale influence. So, separate physical processes are defined by the nonlocal elasticity theory and Eringen's strain gradient theory. To depict nonlocality, the nonlocal strain gradient theory (NSGT) takes into account both of these separate factors at the same time.^[42,43] According to another study,^[42] the following equations represent the σ and $\sigma^{(h)}$ stress tensors in NSGT

$$\sigma = \int_V \alpha_0(x', x, e_0 a) \mathbf{C} : \varepsilon'(x') dV' \quad (12a)$$

$$\sigma^{(h)} = l_m^2 \int_V \alpha_1(x', x, e_1 a) \mathbf{C} : \nabla \varepsilon'(x') dV' \quad (12b)$$

Separate locations are occupied by the classical kernel and the higher-order nonlocal functions α_0 and α_1 . Furthermore, the vector ∇ represents the fourth-order material coefficient, whereas \mathbf{C} stands for the Laplacian operator ($\nabla = \partial/\partial x + \partial/\partial y$). Both $\nabla \varepsilon$ and ε denote the strain gradient and the classical strain tensors, respectively. Furthermore, the material coefficients e_1 and e_0 are indicated by the nonlocality constants, whereas the geometrical properties of atomic bonds are denoted by a . The material size parameter is represented by the letter l_m , and the double-dot product of the tensor is denoted by the colon symbol “:”. This leads us to the following representation of the full stress tensor obtained from the NSGT.^[42,44]

$$\sigma^t = \sigma - \nabla^2 \sigma^{(1)} \quad (13)$$

Assuming compatible $\alpha_1(x', x, e_1 a)$ and $\alpha_0(x', x, e_0 a)$ notions with ref. [45], equaling $e_0 = e_1 = e_0 a$, and utilizing the linear differentiation operator to Equation (2–8) give

$$[1 - (e_0 a)^2 \nabla^2] \sigma = \mathbf{C} : \varepsilon \quad (14a)$$

$$[1 - (e_0 a)^2 \nabla^2] \sigma^{(1)} = l_m^2 \mathbf{C} : \nabla \varepsilon \quad (14b)$$

Equation (4–6) may be used to get the following total stress

$$[1 - (e_0 a)^2 \nabla^2] \sigma = \mathbf{C} : \varepsilon - l_m^2 \nabla \mathbf{C} : \nabla \varepsilon \quad (15)$$

The plate's stress-strain relations are determined by^[42,43]

$$\begin{aligned} [1 - (e_0 a)^2 \nabla^2] \sigma_{xx} &= [1 - l_m^2 \nabla^2] E(z) \varepsilon_{xx} \\ [1 - (e_0 a)^2 \nabla^2] \sigma_{yy} &= [1 - l_m^2 \nabla^2] E(z) \varepsilon_{yy} \\ [1 - (e_0 a)^2 \nabla^2] \sigma_{xz} &= [1 - l_m^2 \nabla^2] G(z) \gamma_{xz} \\ [1 - (e_0 a)^2 \nabla^2] \sigma_{yz} &= [1 - l_m^2 \nabla^2] G(z) \gamma_{yz} \end{aligned} \quad (16)$$

where respectively, σ_{xx} , σ_{yy} and ε_{xx} , ε_{yy} denote the usual stresses and strains in the x and y directions. Additionally, the shear stresses and strains in the xz - and yz -planes are represented by σ_{xz} , σ_{yz} , and γ_{xz} , γ_{yz} . $E(z)$ and $G(z)$ represent elasticity and shear modulus, respectively. When the l_m and $e_0 a$ an in Equation (16) are equal to 0, the stress-strain relations of the classical continuum theory may be found.^[45] Finally, considering the MEE characteristics, the constitutive equations of the NSGT microplate under thermal loads may be set up as in the following structure.

$$\begin{aligned} \sigma(x, y, z)(1 - e_0 a^2 \nabla^2) &= (1 - l_m^2 \nabla^2) [\bar{\mathbf{Q}}(z) \boldsymbol{\varepsilon} - \bar{\boldsymbol{\varepsilon}}(z) \mathbf{E} - \bar{\boldsymbol{\eta}}(z) \mathbf{H}] \\ &\quad - \bar{\mathbf{Q}}(z) \boldsymbol{\alpha}(z) \Delta T \\ D_E(x, y, z)(1 - e_0 a^2 \nabla^2) &= (1 - l_m^2 \nabla^2) [\bar{\boldsymbol{\varepsilon}}^T(z) \boldsymbol{\varepsilon} - \bar{\boldsymbol{\xi}}(z) \mathbf{E} + \bar{\boldsymbol{\zeta}}(z) \mathbf{H}] \\ &\quad - \bar{\mathbf{p}}(z) \Delta T \\ B_M(x, y, z)(1 - e_0 a^2 \nabla^2) &= (1 - l_m^2 \nabla^2) [\bar{\boldsymbol{\eta}}^T(z) \boldsymbol{\varepsilon} + \bar{\boldsymbol{\xi}}(z) \mathbf{E} + \bar{\boldsymbol{\chi}}(z) \mathbf{H}] \\ &\quad - \bar{\boldsymbol{\lambda}}(z) \Delta T \end{aligned} \quad (17)$$

2.5. Displacement Fields and Strains

When applied to a three-layer rectangular plate, the sinusoidal higher-order shear deformation theory (SHSDT) relies on the following assumptions:^[24] 1) Since the displacements are minimal compared to the thickness of the plate, the related stresses are extremely minor; 2) The plane displacements u and v consist of three components: extension u_0 , shear w_s , and bending w_0 ; 3) To incorporate the bending w_0 , shear w_s , and stretching w_{st} components of the transverse stresses (σ_{xz} , σ_{yz} , σ_{zz}) and strains (ε_{xz} , ε_{yz} , ε_{zz}), the transverse displacement w is adjusted; and 4) The trigonometric variation of the shear stresses (σ_{xz} , σ_{yz}) and strains (ε_{xz} , ε_{yz}) over the plate's thickness is increased when shear components (w_s in u , v in-plane, and w transverse displacements) are included. This means that there are no shear stresses (σ_{xz} , σ_{yz}) acting on the top and bottom faces of the plate.

The following is a definition of the nanoplate's displacement field, taking into account the assumptions made for the entire form of the SHSDT.

$$u(x, y, z, t) = u_0(x, y, t) - z \frac{\partial w_0(x, y, t)}{\partial x} - f(z) \frac{\partial w_s(x, y, t)}{\partial x} \quad (18a)$$

$$v(x, y, z, t) = v_0(x, y, t) - z \frac{\partial w_0(x, y, t)}{\partial y} - f(z) \frac{\partial w_s(x, y, t)}{\partial y} \quad (18b)$$

$$w(x, y, z, t) = w_0(x, y, t) + w_s(x, y, t) + w_{st}(x, y, z, t) \quad (18c)$$

Here $f(z)$, w_{st} and $g(z)$ defined as

$$f(z) = z - \frac{H_1}{\pi} \sin\left(\frac{\pi z}{H_1}\right) \quad (19)$$

$$w_{st}(x, y, z, t) = g(z)\varnothing(x, y, t) \quad (20)$$

$$g(z) = \cos\left(\frac{\pi z}{H_1}\right) \quad (21)$$

All displacements of a point inside an unchanged body are represented by the variables u , v , and w in the displacement equations that were described earlier. For every given time t , the in-plane and transverse displacements of a point on the midplane of the undeformed plate $(x, y, 0)$ are represented by u_0 , v_0 , and w_0 , respectively. Here, the bending deflection of the plate is denoted by the w displacement, while the u and v displacements are associated with its extensional deformation. A general form for the strain-displacement interactions associated with the displacement field in Equation (10) is as follows.

$$\begin{Bmatrix} \varepsilon_{xx} \\ \varepsilon_{yy} \\ 2\varepsilon_{xy} \end{Bmatrix} = \begin{Bmatrix} \varepsilon_{xx}^{(0)} \\ \varepsilon_{yy}^{(0)} \\ \gamma_{xy}^{(0)} \end{Bmatrix} + z \begin{Bmatrix} \varepsilon_{xx}^{(b)} \\ \varepsilon_{yy}^{(b)} \\ \gamma_{xy}^{(b)} \end{Bmatrix} + f(z) \begin{Bmatrix} \varepsilon_{xx}^{(s)} \\ \varepsilon_{yy}^{(s)} \\ \gamma_{xy}^{(s)} \end{Bmatrix} \quad (22a)$$

$$\begin{Bmatrix} 2\varepsilon_{xz} \\ 2\varepsilon_{yz} \end{Bmatrix} = g(z) \begin{Bmatrix} \gamma_{xz}^{(0)} \\ \gamma_{yz}^{(0)} \end{Bmatrix} \quad (22b)$$

$$\varepsilon_{zz} = g'(z)\varepsilon_{zz}^{(0)} \quad (22c)$$

Also, the particular strain components are as follows.

$$\begin{Bmatrix} \varepsilon_{xx}^{(0)} \\ \varepsilon_{yy}^{(0)} \\ \gamma_{xy}^{(0)} \end{Bmatrix} = \begin{Bmatrix} \frac{\partial u_0}{\partial x} \\ \frac{\partial v_0}{\partial y} \\ \frac{\partial u_0}{\partial y} + \frac{\partial v_0}{\partial x} \end{Bmatrix}, \quad \begin{Bmatrix} \varepsilon_{xx}^{(b)} \\ \varepsilon_{yy}^{(b)} \\ \gamma_{xy}^{(b)} \end{Bmatrix} = \begin{Bmatrix} -\frac{\partial^2 w_0}{\partial x^2} \\ -\frac{\partial^2 w_0}{\partial y^2} \\ -2\frac{\partial^2 w_0}{\partial x \partial y} \end{Bmatrix} \quad (23a)$$

$$\begin{Bmatrix} \varepsilon_{xx}^{(s)} \\ \varepsilon_{yy}^{(s)} \\ \gamma_{xy}^{(s)} \end{Bmatrix} = \begin{Bmatrix} -\frac{\partial^2 w_s}{\partial x^2} \\ -\frac{\partial^2 w_s}{\partial y^2} \\ -2\frac{\partial^2 w_s}{\partial x \partial y} \end{Bmatrix} \quad (23b)$$

$$\begin{Bmatrix} \gamma_{xz}^{(0)} \\ \gamma_{yz}^{(0)} \\ \varepsilon_{zz}^{(0)} \end{Bmatrix} = \begin{Bmatrix} (1-f'(z))\frac{\partial w_s}{\partial x} + g(z)\frac{\partial \varnothing}{\partial x} \\ (1-f'(z))\frac{\partial w_s}{\partial y} + g(z)\frac{\partial \varnothing}{\partial y} \\ \varnothing \end{Bmatrix} = \begin{Bmatrix} g(z)\left(\frac{\partial w_s}{\partial x} + \frac{\partial \varnothing}{\partial x}\right) \\ g(z)\left(\frac{\partial w_s}{\partial y} + \frac{\partial \varnothing}{\partial y}\right) \\ \varnothing \end{Bmatrix} \quad (23c)$$

2.6. Constitutive Equations

Applying the nonlocal and strain-gradient differential operators, the constitutive relations of the surface layers are described by^[46] $\mathcal{L}(\ast) \equiv 1 - (e_0 a)^2 \nabla^2$ and $\Gamma(\ast) \equiv 1 - (l_m)^2 \nabla^2$.

$$\begin{Bmatrix} \mathcal{L}(\sigma_{xx}^s) \\ \mathcal{L}(\sigma_{yy}^s) \\ \mathcal{L}(\sigma_{zz}^s) \\ \mathcal{L}(\sigma_{yz}^s) \\ \mathcal{L}(\sigma_{xz}^s) \\ \mathcal{L}(\sigma_{xy}^s) \end{Bmatrix} = \Gamma \begin{bmatrix} C_{11}^s & C_{12}^s & C_{13}^s & 0 & 0 & 0 \\ C_{12}^s & C_{22}^s & C_{23}^s & 0 & 0 & 0 \\ C_{13}^s & C_{23}^s & C_{33}^s & 0 & 0 & 0 \\ 0 & 0 & 0 & C_{44}^s & 0 & 0 \\ 0 & 0 & 0 & 0 & C_{55}^s & 0 \\ 0 & 0 & 0 & 0 & 0 & C_{66}^s \end{bmatrix} \times \begin{Bmatrix} \varepsilon_{xx} \\ \varepsilon_{yy} \\ \varepsilon_{zz} \\ 2\varepsilon_{yz} \\ 2\varepsilon_{xz} \\ 2\varepsilon_{xy} \end{Bmatrix} - \Gamma \begin{bmatrix} 0 & 0 & e_{31} \\ 0 & 0 & e_{32} \\ 0 & 0 & e_{33} \\ 0 & e_{24} & 0 \\ e_{15} & 0 & 0 \\ 0 & 0 & 0 \end{bmatrix} \begin{Bmatrix} E_x \\ E_y \\ E_z \end{Bmatrix} \quad (24a)$$

$$- \Gamma \begin{bmatrix} 0 & 0 & q_{31} \\ 0 & 0 & q_{32} \\ 0 & 0 & q_{33} \\ 0 & q_{24} & 0 \\ q_{15} & 0 & 0 \\ 0 & 0 & 0 \end{bmatrix} \begin{Bmatrix} H_x \\ H_y \\ H_z \end{Bmatrix}$$

$$\begin{Bmatrix} \mathcal{L}(D_x) \\ \mathcal{L}(D_y) \\ \mathcal{L}(D_z) \end{Bmatrix} = \Gamma \begin{bmatrix} 0 & 0 & 0 & 0 & e_{15} & 0 \\ 0 & 0 & 0 & e_{24} & 0 & 0 \\ e_{31} & e_{32} & e_{33} & 0 & 0 & 0 \end{bmatrix} \begin{Bmatrix} \varepsilon_{xx} \\ \varepsilon_{yy} \\ \varepsilon_{zz} \\ 2\varepsilon_{yz} \\ 2\varepsilon_{xz} \\ 2\varepsilon_{xy} \end{Bmatrix} \quad (24b)$$

$$+ \Gamma \begin{bmatrix} \varepsilon_{11} & 0 & 0 \\ 0 & \varepsilon_{22} & 0 \\ 0 & 0 & \varepsilon_{33} \end{bmatrix} \begin{Bmatrix} E_x \\ E_y \\ E_z \end{Bmatrix}$$

$$+ \Gamma \begin{bmatrix} g_{11} & 0 & 0 \\ 0 & g_{22} & 0 \\ 0 & 0 & g_{33} \end{bmatrix} \begin{Bmatrix} H_x \\ H_y \\ H_z \end{Bmatrix}$$

$$\begin{Bmatrix} \mathcal{L}(B_x) \\ \mathcal{L}(B_y) \\ \mathcal{L}(B_z) \end{Bmatrix} = \Gamma \begin{bmatrix} 0 & 0 & 0 & 0 & q_{15} & 0 \\ 0 & 0 & 0 & q_{24} & 0 & 0 \\ q_{31} & q_{32} & q_{33} & 0 & 0 & 0 \end{bmatrix} \begin{Bmatrix} \varepsilon_{xx} \\ \varepsilon_{yy} \\ \varepsilon_{zz} \\ 2\varepsilon_{yz} \\ 2\varepsilon_{xz} \\ 2\varepsilon_{xy} \end{Bmatrix} \quad (24c)$$

$$+ \Gamma \begin{bmatrix} \varepsilon_{11} & 0 & 0 \\ 0 & \varepsilon_{22} & 0 \\ 0 & 0 & \varepsilon_{33} \end{bmatrix} \begin{Bmatrix} E_x \\ E_y \\ E_z \end{Bmatrix}$$

$$+ \Gamma \begin{bmatrix} \mu_{11} & 0 & 0 \\ 0 & \mu_{22} & 0 \\ 0 & 0 & \mu_{33} \end{bmatrix} \begin{Bmatrix} H_x \\ H_y \\ H_z \end{Bmatrix}$$

By establishing the electric $\check{\varphi}$ and magnetic potentials $\check{\psi}$, the constitutive relations may be defined in their entirety. The components of electric E_i and magnetic fields H_i are expressed using these 3D potentials.

$$E_i = \{-\check{\varphi}, i\}, \quad H_i = \{-\check{\psi}, i\}, \quad i = x, y, z \quad (25)$$

According to Maxwell's equations, the distributions of these potentials for a nanoplate activated with initial external electric φ_0 and magnetic ψ_0 potentials are characterized by fusing the linear and cosine functions as in the following.^[47,48]

$$\begin{Bmatrix} \check{\varphi}(x, y, z, t) \\ \check{\psi}(x, y, z, t) \end{Bmatrix} = \begin{Bmatrix} \check{\varphi}_0 \\ \check{\psi}_0 \end{Bmatrix} \frac{2\hat{z}}{H_t} - \begin{Bmatrix} \varphi(x, y, t) \\ \psi(x, y, t) \end{Bmatrix} \cos\left(\frac{\pi\hat{z}}{H_t}\right) \quad (26)$$

Here $\varphi(x, y, t)$ and $\psi(x, y, t)$, in turn, imply the time-dependent planar electric and magnetic potential distributions. Furthermore, the \hat{z} variable stands for the thickness of the surface-layers ($\hat{z} = z \pm h/2 \pm h_s/2$). For the plate's top layer, \hat{z} is defined as ($\hat{z} \equiv z_1 = z - h/2 - h_s/2$), whereas \hat{z} is defined as ($\hat{z} \equiv z_2 = z + h/2 + h_s/2$) for the plate's bottom layer. Note that, z is only valid for ($h/2 \leq z \leq h/2 + h_s/2$) and ($-h/2 - h_s/2 \leq z \leq -h/2$).

For the rim layer between the auxetic core and face layers, the constitutive equations can be described by

$$\begin{Bmatrix} \mathcal{L}(\sigma_{xx}^r) \\ \mathcal{L}(\sigma_{yy}^r) \\ \mathcal{L}(\sigma_{zz}^r) \\ \mathcal{L}(\sigma_{yz}^r) \\ \mathcal{L}(\sigma_{xz}^r) \\ \mathcal{L}(\sigma_{xy}^r) \end{Bmatrix} = \Gamma \begin{bmatrix} C_{11}^r & C_{12}^r & C_{13}^r & 0 & 0 & 0 \\ C_{12}^r & C_{22}^r & C_{23}^r & 0 & 0 & 0 \\ C_{13}^r & C_{23}^r & C_{33}^r & 0 & 0 & 0 \\ 0 & 0 & 0 & C_{44}^r & 0 & 0 \\ 0 & 0 & 0 & 0 & C_{55}^r & 0 \\ 0 & 0 & 0 & 0 & 0 & C_{66}^r \end{bmatrix} \begin{Bmatrix} \varepsilon_{xx} \\ \varepsilon_{yy} \\ \varepsilon_{zz} \\ 2\varepsilon_{yz} \\ 2\varepsilon_{xz} \\ 2\varepsilon_{xy} \end{Bmatrix} \quad (27)$$

For the auxetic core layer, the constitutive equations can be described by

$$\begin{Bmatrix} \mathcal{L}(\sigma_{xx}^c) \\ \mathcal{L}(\sigma_{yy}^c) \\ \mathcal{L}(\sigma_{zz}^c) \\ \mathcal{L}(\sigma_{yz}^c) \\ \mathcal{L}(\sigma_{xz}^c) \\ \mathcal{L}(\sigma_{xy}^c) \end{Bmatrix} = \Gamma \begin{bmatrix} C_{11}^c & C_{12}^c & C_{13}^c & 0 & 0 & 0 \\ C_{12}^c & C_{22}^c & C_{23}^c & 0 & 0 & 0 \\ C_{13}^c & C_{23}^c & C_{33}^c & 0 & 0 & 0 \\ 0 & 0 & 0 & C_{44}^c & 0 & 0 \\ 0 & 0 & 0 & 0 & C_{55}^c & 0 \\ 0 & 0 & 0 & 0 & 0 & C_{66}^c \end{bmatrix} \begin{Bmatrix} \varepsilon_{xx} \\ \varepsilon_{yy} \\ \varepsilon_{zz} \\ 2\varepsilon_{yz} \\ 2\varepsilon_{xz} \\ 2\varepsilon_{xy} \end{Bmatrix} \quad (28)$$

Here C_{ij}^n stands for the stiffness coefficients and is defined by

$$C_{11}^c = \frac{1-\nu}{\nu} \lambda(z) \quad (29a)$$

$$C_{12}^c = \lambda(z) \quad (29b)$$

$$C_{66}^c = \mu(z) \quad (29c)$$

$$C_{11}^c = C_{22}^c = C_{33}^c \quad (29d)$$

$$C_{12}^c = C_{13}^c = C_{23}^c \quad (29e)$$

$$C_{44}^c = C_{55}^c = C_{66}^c \quad (29f)$$

In stiffness coefficients, the $\lambda(z)$ and $\mu(z)$ are the Lamé constants. ($\lambda(z) = \frac{\nu E(z)}{(1+\nu)(1-2\nu)}$, $\mu(z) = \frac{E(z)}{2(1+\nu)}$) ν and $E(z)$ are derived from the elasticity and Poisson ratio terms of the auxetic core given in Equation (2–8).

2.7. Equations of Motion

Using the following virtual displacements, Hamilton's principle may be altered for the motion equations of the three-layered rectangular nanoplate^[49]

$$\int_0^T (\delta\mathcal{U} - \delta\mathcal{E} - \delta\mathcal{M} - \delta\mathcal{K} + \delta\mathcal{V}) dt = 0 \quad (30)$$

Here, $\delta\mathcal{U}$, $\delta\mathcal{K}$, and $\delta\mathcal{V}$ are, in turn, the virtual forms of strain energy, kinetic energy, and work done by external forces. Additionally, $\delta\mathcal{E}$ and $\delta\mathcal{M}$ are the electric and magnetic fields' virtual contributions. Accordingly, the virtual strain energy $\delta\mathcal{U}$ is defined by

$$\begin{aligned} \delta\mathcal{U} = & \int_{\Omega} \left[\int_{h_0}^{h_1} (\sigma_{xx}^f \delta\varepsilon_{xx} + \sigma_{yy}^f \delta\varepsilon_{yy} + \sigma_{zz}^f \delta\varepsilon_{zz} + 2\sigma_{yz}^f \delta\varepsilon_{yz} \right. \\ & + 2\sigma_{xz}^f \delta\varepsilon_{xz} + 2\sigma_{xy}^f \delta\varepsilon_{xy}) dz \\ & + \int_{h_1}^{h_2} (\sigma_{xx}^r \delta\varepsilon_{xx} + \sigma_{yy}^r \delta\varepsilon_{yy} + \sigma_{zz}^r \delta\varepsilon_{zz} + 2\sigma_{yz}^r \delta\varepsilon_{yz} \\ & + 2\sigma_{xz}^r \delta\varepsilon_{xz} + 2\sigma_{xy}^r \delta\varepsilon_{xy}) dz \\ & + \int_{h_2}^{h_3} (\sigma_{xx}^c \delta\varepsilon_{xx} + \sigma_{yy}^c \delta\varepsilon_{yy} + \sigma_{zz}^c \delta\varepsilon_{zz} + 2\sigma_{yz}^c \delta\varepsilon_{yz} \\ & + 2\sigma_{xz}^c \delta\varepsilon_{xz} + 2\sigma_{xy}^c \delta\varepsilon_{xy}) dz \\ & + \int_{h_3}^{h_4} (\sigma_{xx}^f \delta\varepsilon_{xx} + \sigma_{yy}^f \delta\varepsilon_{yy} + \sigma_{zz}^f \delta\varepsilon_{zz} + 2\sigma_{yz}^f \delta\varepsilon_{yz} \\ & + 2\sigma_{xz}^f \delta\varepsilon_{xz} + 2\sigma_{xy}^f \delta\varepsilon_{xy}) dz \\ & \left. + \int_{h_4}^{h_5} ((\sigma_{xx}^f \delta\varepsilon_{xx} + \sigma_{yy}^f \delta\varepsilon_{yy} + \sigma_{zz}^f \delta\varepsilon_{zz} + 2\sigma_{yz}^f \delta\varepsilon_{yz} \right. \\ & \left. + 2\sigma_{xz}^f \delta\varepsilon_{xz} + 2\sigma_{xy}^f \delta\varepsilon_{xy}) dz \right] dx dy \end{aligned} \quad (31)$$

Additionally, the electric $\delta\mathcal{E}$ and magnetic $\delta\mathcal{M}$ fields' contributions are given by

$$\delta\mathcal{E} = \int_{\Omega} \left[\int_{h_0}^{h_1} (D_x \delta E_x + D_y \delta E_y + D_z \delta E_z) dz + \int_{h_4}^{h_5} (D_x \delta E_x + D_y \delta E_y + D_z \delta E_z) dz \right] dx dy \quad (32)$$

$$\delta\mathcal{M} = \int_{\Omega} \left[\int_{h_0}^{h_1} (B_x \delta H_x + B_y \delta H_y + B_z \delta H_z) dz + \int_{h_4}^{h_5} (B_x \delta H_x + B_y \delta H_y + B_z \delta H_z) dz \right] dx dy \quad (33)$$

Also, the contribution of the kinetic energy is as follows.

$$\delta\mathcal{K} = \int_{\Omega} \left[\int_{h_1}^{h_2} \rho^f (\dot{u}\delta\dot{u} + \dot{v}\delta\dot{v} + \dot{w}\delta\dot{w}) dz + \int_{h_2}^{h_3} \rho^r (\dot{u}\delta\dot{u} + \dot{v}\delta\dot{v} + \dot{w}\delta\dot{w}) dz + \int_{h_3}^{h_4} \rho^c (\dot{u}\delta\dot{u} + \dot{v}\delta\dot{v} + \dot{w}\delta\dot{w}) dz + \int_{h_4}^{h_5} \rho^r (\dot{u}\delta\dot{u} + \dot{v}\delta\dot{v} + \dot{w}\delta\dot{w}) dz + \int_{h_5}^{h_6} \rho^f (\dot{u}\delta\dot{u} + \dot{v}\delta\dot{v} + \dot{w}\delta\dot{w}) dz \right] dx dy \quad (34)$$

Here $\rho^f(z)$, $\rho^r(z)$, and $\rho^c(z)$, in turn, stand for the mass densities of nanoplate's surface layers, rim layer, and core layer. The mass density $\rho^c(z)$ of the core layer has been obtained by Equation (2–8). Additionally, a variable's time derivative is implied by a dot superscript, such as in the expression $\dot{u} = \partial u / \partial t$. The following summarizes how in-plane external pressures contribute to virtual work.

$$\delta\mathcal{V} = - \int_{\Omega} \left[(N_{xx0} + N_{xx\mathcal{E}} + N_{xx\mathcal{M}}) \frac{\partial w_0}{\partial x} \frac{\partial \delta w_0}{\partial x} + (N_{yy0} + N_{yy\mathcal{E}} + N_{yy\mathcal{M}}) \frac{\partial w_0}{\partial y} \frac{\partial \delta w_0}{\partial y} \right] dx dy \quad (35)$$

The 0, \mathcal{E} , and \mathcal{M} subscripts represent the in-plane compressive mechanical, electrical, and magnetic forces. Clearly, $N_{xx0} = P_{x0}$ and $N_{yy0} = P_{y0}$ are compressive mechanical forces, $N_{xx\mathcal{M}} = P_{q31}$ and $N_{yy\mathcal{M}} = P_{q32}$ are the magnetic forces arising from magnetic potential, and $N_{xx\mathcal{E}} = P_{e31}$ and $N_{yy\mathcal{E}} = P_{e32}$ are the electric forces resulting from the external electric voltage. The virtual work equation disregards the mechanical forces applied to the top and lower surfaces since the study only looks at MEE nanoplates' free vibration and buckling responses. Assume that the plate buckles with cylindrical bending behavior when an external force is applied along its midplane. Only the deflection's bending (w_0) component is connected to the externally applied axial forces. Additionally, the overall behavior of the plate will be influenced by the deflection's shear (w_s) and stretch (w_{st}) components. The resulting forces and moments that are linked to thickness may then be expressed as follows.

$$\begin{Bmatrix} N_{xx} & N_{yy} & N_{xy} \\ M_{xx}^{(b)} & M_{yy}^{(b)} & M_{xy}^{(b)} \\ M_{xx}^{(s)} & M_{yy}^{(s)} & M_{xy}^{(s)} \end{Bmatrix} = \int_{h_1}^{h_2} (\sigma_{xx}^f, \sigma_{yy}^f, \sigma_{xy}^f) \begin{Bmatrix} 1 \\ z \\ f(z) \end{Bmatrix} dz + \int_{h_2}^{h_3} (\sigma_{xx}^r, \sigma_{yy}^r, \sigma_{xy}^r) \begin{Bmatrix} 1 \\ z \\ f(z) \end{Bmatrix} dz + \int_{h_3}^{h_4} (\sigma_{xx}^c, \sigma_{yy}^c, \sigma_{xy}^c) \begin{Bmatrix} 1 \\ z \\ f(z) \end{Bmatrix} dz + \int_{h_4}^{h_5} (\sigma_{xx}^r, \sigma_{yy}^r, \sigma_{xy}^r) \begin{Bmatrix} 1 \\ z \\ f(z) \end{Bmatrix} dz + \int_{h_5}^{h_6} (\sigma_{xx}^f, \sigma_{yy}^f, \sigma_{xy}^f) \begin{Bmatrix} 1 \\ z \\ f(z) \end{Bmatrix} dz \quad (36a)$$

$$N_{zz} = \int_{-h/2-h_s}^{h/2} \sigma_{zz}^s g'(z) dz + \int_{-h/2}^{h/2} \sigma_{zz}^c g'(z) dz + \int_{h/2}^{h/2+h_s} \sigma_{zz}^s g'(z) dz \quad (36b)$$

$$\{S_{xz}, S_{yz}\} = \int_{-h/2-h_s}^{-h/2} \{\sigma_{xz}^s, \sigma_{yz}^s\} g(z) dz + \int_{-h/2}^{h/2} \{\sigma_{xz}^c, \sigma_{yz}^c\} g(z) dz + \int_{h/2}^{h/2+h_s} \{\sigma_{xz}^s, \sigma_{yz}^s\} g(z) dz \quad (36c)$$

Also, the virtual strain energy gets the following form.

$$\delta U = \int_{\Omega} \left(N_{xx} \delta \varepsilon_{xx}^{(0)} + N_{yy} \delta \varepsilon_{yy}^{(0)} + N_{zz} \delta \varepsilon_{zz}^{(0)} + N_{xy} \delta \varepsilon_{xy}^{(0)} + N_{xz} \delta \varepsilon_{xz}^{(0)} + N_{yz} \delta \varepsilon_{yz}^{(0)} + M_{xx} \delta \varepsilon_{xx}^{(b)} + M_{yy} \delta \varepsilon_{yy}^{(b)} + M_{xy} \delta \varepsilon_{xy}^{(b)} + M_{xx} \delta \varepsilon_{xx}^{(s)} + M_{yy} \delta \varepsilon_{yy}^{(s)} + M_{xy} \delta \varepsilon_{xy}^{(s)} \right) dx dy \quad (37)$$

Additionally, the thickness-related electric $\bar{D}_i (i = x, y, z)$ and magnetic $\bar{B}_i (i = x, y, z)$ coefficients are given as

$$\{\bar{D}_x, \bar{D}_y, \bar{D}_z\} = \int_{h_1}^{h_2} (D_x, D_y, D_z) \begin{Bmatrix} \cos\left(\frac{\pi z_2}{h_s}\right) \\ \cos\left(\frac{\pi z_2}{h_s}\right) \\ \frac{\pi}{h_s} \sin\left(\frac{\pi z_2}{h_s}\right) \end{Bmatrix} dz + \int_{h_5}^{h_6} (D_x, D_y, D_z) \begin{Bmatrix} \cos\left(\frac{\pi z_2}{h}\right) \\ \cos\left(\frac{\pi z_2}{h}\right) \\ \frac{\pi}{h} \sin\left(\frac{\pi z_2}{h}\right) \end{Bmatrix} dz \quad (38)$$

$$\{\bar{B}_x, \bar{B}_y, \bar{B}_z\} = \int_{h_1}^{h_2} (B_x, B_y, B_z) \begin{Bmatrix} \cos\left(\frac{\pi z_2}{h_s}\right) \\ \cos\left(\frac{\pi z_2}{h_s}\right) \\ \frac{\pi}{h_s} \sin\left(\frac{\pi z_2}{h_s}\right) \end{Bmatrix} dz \quad (39)$$

$$+ \int_{h_5}^{h_6} (B_x, B_y, B_z) \begin{Bmatrix} \cos\left(\frac{\pi z_2}{h}\right) \\ \cos\left(\frac{\pi z_2}{h}\right) \\ \frac{\pi}{h} \sin\left(\frac{\pi z_2}{h}\right) \end{Bmatrix} dz$$

The electric and magnetic fields' virtual contribution can be presented in an easier form.

$$\delta\mathcal{E} = \int_{\Omega} \left(\bar{D}_x \frac{\partial \delta\varphi}{\partial x} + \bar{D}_y \frac{\partial \delta\varphi}{\partial y} - \bar{D}_z \delta\varphi \right) dx dy \quad (40)$$

$$\delta\mathcal{M} = \int_{\Omega} \left(\bar{B}_x \frac{\partial \delta\psi}{\partial x} + \bar{B}_y \frac{\partial \delta\psi}{\partial y} - \bar{B}_z \delta\psi \right) dx dy \quad (41)$$

The kinetic energy variation defined by the m_i mass inertias can be written as

$$\delta\mathcal{K} = \int_{\Omega} \left[\begin{aligned} & m_0 (\dot{u}_0 \delta \dot{u}_0 + \dot{v}_0 \delta \dot{v}_0 + \dot{w}_0 \delta \dot{w}_0 + \dot{w}_s \delta \dot{w}_s \\ & + \dot{w}_s \delta \dot{w}_0 + \dot{w}_s \delta \dot{w}_s) \\ & - m_1 \left(\dot{u}_0 \frac{\partial \delta \dot{u}_0}{\partial x} + \frac{\partial \dot{w}_0}{\partial x} \delta \dot{u}_0 + \dot{v}_0 \frac{\partial \delta \dot{w}_0}{\partial y} + \frac{\partial \dot{w}_0}{\partial y} \delta \dot{v}_0 \right) \\ & \times \left(\frac{\partial \dot{w}_0}{\partial x} \frac{\partial \delta \dot{w}_0}{\partial x} + \frac{\partial \dot{w}_0}{\partial y} \frac{\partial \delta \dot{w}_0}{\partial y} \right) \\ & - m_3 \left(\dot{u}_0 \frac{\partial \delta \dot{w}_0}{\partial x} + \frac{\partial \dot{w}_0}{\partial x} \delta \dot{u}_0 + \dot{v}_0 \frac{\partial \delta \dot{w}_0}{\partial y} + \frac{\partial \dot{w}_0}{\partial y} \delta \dot{v}_0 \right) \\ & + m_4 \left(\frac{\partial \dot{w}_0}{\partial x} \frac{\partial \delta \dot{w}_0}{\partial x} + \frac{\partial \dot{w}_0}{\partial x} \frac{\partial \delta \dot{w}_0}{\partial x} + \frac{\partial \dot{w}_0}{\partial y} \frac{\partial \delta \dot{w}_0}{\partial y} \right. \\ & \left. + \frac{\partial \dot{w}_0}{\partial y} \frac{\partial \delta \dot{w}_0}{\partial y} \right) m_5 \left(\frac{\partial \dot{w}_s}{\partial x} \frac{\partial \delta \dot{w}_s}{\partial x} + \frac{\partial \dot{w}_s}{\partial y} \frac{\partial \delta \dot{w}_s}{\partial y} \right) \\ & \left. + m_6 (\dot{w}_0 \delta \dot{\phi} + \dot{w}_s \delta \dot{\phi} + \dot{\phi} \delta \dot{w}_0 + \dot{\phi} \delta \dot{w}_s) + m_7 \dot{\phi} \delta \dot{\phi} \right] dx dy \quad (42)$$

The differentiation of variables concerning time is shown here by the dot superscript, and $m_i (i=0, 1, 2)$ mass inertias are defined as

$$m_i = \int_{h_1}^{h_2} \rho^f z^i dz + \int_{h_2}^{h_3} \rho^r z^i dz + \int_{h_3}^{h_4} p^c(z) z^i dz \quad (43a)$$

$$+ \int_{h_4}^{h_5} \rho^r z^i dz + \int_{h_5}^{h_6} \rho^f z^i dz$$

$$m_{i+3} = \int_{h_1}^{h_2} \rho^f f(z) z^i dz + \int_{h_2}^{h_3} \rho^r f(z) z^i dz + \int_{h_3}^{h_4} p^c(z) f(z) z^i dz \quad (43b)$$

$$+ \int_{h_4}^{h_5} \rho^r f(z) z^i dz + \int_{h_5}^{h_6} \rho^f f(z) z^i dz$$

$$m_6 = \int_{h_1}^{h_2} \rho^f g(z) dz + \int_{h_2}^{h_3} \rho^r g(z) dz + \int_{h_3}^{h_4} p^c(z) g(z) dz \quad (43c)$$

$$+ \int_{h_4}^{h_5} \rho^r g(z) dz + \int_{h_5}^{h_6} \rho^f g(z) dz$$

$$m_7 = \int_{h_1}^{h_2} \rho^f g^2(z) dz + \int_{h_2}^{h_3} \rho^r g^2(z) dz + \int_{h_3}^{h_4} p^c(z) g^2(z) dz \quad (43d)$$

$$+ \int_{h_4}^{h_5} \rho^r g^2(z) dz + \int_{h_5}^{h_6} \rho^f g^2(z) dz$$

The virtual work's latest form resulting from in-plane external forces is given by

$$\delta\mathcal{V} = \int_{\Omega} \left[(p_{x0} + p_{e31} + p_{q31}) \frac{\partial w_0}{\partial x} \frac{\partial \delta w_0}{\partial x} \right. \quad (44)$$

$$\left. + (p_{y0} + p_{e32} + p_{q32}) \frac{\partial w_0}{\partial x} \frac{\partial \delta w_0}{\partial x} \right] dx dy$$

In the analyses, in-plane mechanical compression forces are assumed to be equal, $p_{x0} = N_0$ and $p_{y0} = \gamma N_0$, with $\gamma = p_{x0}/p_{y0}$. The in-plane electric p_{e3i} and magnetic p_{q3i} ($i = 1, 2$) forces are described as

$$p_{e3i} = - \left[\int_{h_1}^{h_2} e_{3i} \left(\frac{2V_0}{h_s} \right) dz + \int_{h_5}^{h_6} e_{3i}(z) \left(\frac{2V_0}{h} \right) dz \right] \quad (45a)$$

$$p_{q3i} = - \left[\int_{h_1}^{h_2} q_{3i} \left(\frac{2H_0}{h_s} \right) dz + \int_{h_5}^{h_6} q_{3i}(z) \left(\frac{2H_0}{h} \right) dz \right] \quad (45b)$$

For a macrorectangular plate based on the SHSDT, the final seven motion Equation (46a–g) can be obtained by substituting the energy variation equations $\delta\mathcal{U}$, $\delta\mathcal{E}$, $\delta\mathcal{M}$, $\delta\mathcal{K}$, and $\delta\mathcal{V}$ from Equation (30) and (31–34) and (33) into Equation (22), performing partial integration to obtain the whole differentiations of generalized virtual translations relative to x , y , and t .

$$\delta u_0 : \frac{\partial N_{xx}}{\partial x} + \frac{\partial N_{xy}}{\partial x} = m_0 \ddot{u}_0 - m_1 \frac{\partial \dot{w}_0}{\partial x} - m_1 \frac{\partial \dot{w}_s}{\partial x} \quad (46a)$$

$$\delta v_0 : \frac{\partial N_{yy}}{\partial y} + \frac{\partial N_{xy}}{\partial x} = m_0 \ddot{v}_0 - m_1 \frac{\partial \dot{w}_0}{\partial y} - m_3 \frac{\partial \dot{w}_s}{\partial y} \quad (46b)$$

$$\delta w_0 : \frac{\partial^2 M_{xx}^{(b)}}{\partial x^2} + 2 \frac{\partial^2 M_{xx}^{(b)}}{\partial x \partial y} + \frac{\partial^2 M_{yy}^{(b)}}{\partial y^2} - (p_{x0} + p_{e31} + p_{q31}) \frac{\partial^2 w_0}{\partial y^2} \quad (46c)$$

$$= m_0 (\ddot{w}_0 + \ddot{w}_s) + m_1 \left(\frac{\partial \ddot{u}_0}{\partial x} + \frac{\partial \ddot{v}_0}{\partial y} \right) - m_2 \left(\frac{\partial \dot{w}_0}{\partial x^2} + \frac{\partial \dot{w}_0}{\partial y^2} \right)$$

$$- m_4 \left(\frac{\partial^2 \dot{w}_s}{\partial x^2} + \frac{\partial^2 \dot{w}_s}{\partial y^2} \right) + m_6 \ddot{\phi}$$

$$\delta w_s : \frac{\partial^2 M_{xx}^{(s)}}{\partial x^2} + 2 \frac{\partial^2 M_{xy}^{(s)}}{\partial x \partial y} + \frac{\partial^2 M_{yy}^{(s)}}{\partial y^2} + \frac{\partial s_{xz}}{\partial x} + \frac{\partial s_{yz}}{\partial y} \quad (46d)$$

$$= m_0 (\ddot{w}_0 + \ddot{w}_s) + m_3 \left(\frac{\partial \ddot{u}_0}{\partial x} + \frac{\partial \ddot{v}_0}{\partial y} \right)$$

$$- m_4 \left(\frac{\partial^2 \dot{w}_0}{\partial x^2} + \frac{\partial^2 \dot{w}_0}{\partial y^2} \right) - m_5 \left(\frac{\partial^2 \dot{w}_s}{\partial x^2} + \frac{\partial^2 \dot{w}_s}{\partial y^2} \right) + m_6 \ddot{\phi}$$

$$\delta\phi: \frac{\partial S_{xz}}{\partial x} + \frac{\partial S_{yz}}{\partial y} - N_{zz} = m_6(\ddot{w}_0 + \ddot{w}_s) + m_7\ddot{\phi} \quad (46e)$$

$$\delta\varphi: \frac{\partial \bar{D}_x}{\partial x} + \frac{\partial \bar{D}_{yz}}{\partial y} + \bar{D}_z = 0 \quad (46f)$$

$$\delta\psi: \frac{\partial \bar{B}_x}{\partial x} + \frac{\partial \bar{B}_{yz}}{\partial y} + \bar{B}_z = 0 \quad (46g)$$

The nanoplate's boundary conditions are defined in the following form.

$$\delta u_0: 0 = N_{xx}n_x + N_{xy}n_y - m_1\ddot{w}_0n_x - m_3\ddot{w}_sn_x \quad (47a)$$

$$\delta v_0: 0 = N_{yy}n_y + N_{xy}n_x - m_1\ddot{w}_0n_y - m_3\ddot{w}_sn_y \quad (47b)$$

$$\begin{aligned} \delta w_0: 0 = & \left[\frac{\partial M_{xx}^{(b)}}{\partial x} + \frac{\partial M_{xy}^{(b)}}{\partial y} - (p_{x0} + p_{\epsilon 31} + p_{q31}) \frac{\partial w_0}{\partial x} \right] n_x \\ & + \left[\frac{\partial M_{yy}^{(b)}}{\partial y} + \frac{\partial M_{xy}^{(b)}}{\partial x} \frac{\partial M_{xy}^{(b)}}{\partial y} - (p_{y0} + p_{\epsilon 32} + p_{q32}) \frac{\partial w_0}{\partial x} \right] n_y \\ & + \left(m_1\ddot{u} - m_2 \frac{\partial \ddot{w}_0}{\partial x} - m_4 \frac{\partial \ddot{w}_s}{\partial x} \right) n_x \\ & + \left(m_1\ddot{v}_0 - m_2 \frac{\partial \ddot{w}_0}{\partial y} - m_4 \frac{\partial \ddot{w}_s}{\partial y} \right) n_y \end{aligned} \quad (47c)$$

$$\delta \frac{\partial w_0}{\partial n}: 0 = M_{nn}^{(b)} \quad (47d)$$

$$\delta \frac{\partial w_s}{\partial n}: 0 = M_{nn}^{(s)} \quad (47e)$$

$$\delta\phi: 0 = S_{xz}n_x + S_{yz}n_y \quad (47f)$$

$$\delta\varphi: 0 = \bar{D}_xn_x + \bar{D}_yn_y \quad (47g)$$

$$\delta\psi: 0 = \bar{B}_xn_x + B_yn_y \quad (47h)$$

Here

$$\begin{aligned} M_{nn}^{(b)} &= M_{xx}^{(b)}n_x^2 + 2M_{xy}^{(b)}n_xn_y + M_{yy}^{(b)}n_y^2, \\ M_{nn}^{(s)} &= M_{xx}^{(s)}n_x^2 + 2M_{xy}^{(s)}n_xn_y + M_{yy}^{(s)}n_y^2 \end{aligned} \quad (47i)$$

Applying the nonlocal and strain-gradient differential operators $\mathcal{L}(\ast) \equiv 1 - (e_0a)^2\nabla^2$ and $\Gamma(\ast) \equiv 1 - (l_m)^2\nabla^2$ and replacing Equation ((10) and (14)–(16) and (19) and (26) and (28)) into Equation (35), the following equilibrium equations (Equation 37a–g) concerning displacements and MEE coefficients can be obtained for a rectangular nanoplate in the following form.

$$\begin{aligned} \Gamma = & \left[\begin{aligned} & A_{11}^{(0)} \frac{\partial^2 u_0}{\partial x^2} - A_{11}^{(1)} \frac{\partial^3 w_0}{\partial x^3} - A_{11}^{-(0)} \frac{\partial^3 w_s}{\partial x^3} + (A_{12}^{(0)} + A_{66}^{(0)}) \frac{\partial v_0}{\partial x \partial y} \\ & - (A_{12}^{(1)} + 2A_{66}^{(1)}) \frac{\partial^3 w_s}{\partial x \partial y^2} - (A_{12}^{-(0)} + 2A_{66}^{-(0)}) \frac{\partial^3 w_s}{\partial x \partial y^2} \\ & + A_{66}^{(0)} \frac{\partial^3 u_0}{\partial y^2} + \tilde{A}_{13}^{(0)} \frac{\partial^3 u_0}{\partial y^2} + \bar{B}_{\epsilon 13}^{(0)} \frac{\partial \varphi}{\partial x} + \bar{B}_{q13}^{(0)} \frac{\partial \psi}{\partial x} \end{aligned} \right] \\ & = \mathcal{L} \left[m_0\ddot{u} - m_1 \frac{\partial \ddot{w}_0}{\partial x} - m_3 \frac{\partial \ddot{w}_s}{\partial x} \right] \end{aligned} \quad (48a)$$

$$\begin{aligned} \Gamma = & \left[\begin{aligned} & A_{22}^{(0)} \frac{\partial^2 v_0}{\partial y^2} - A_{22}^{(1)} \frac{\partial^3 w_0}{\partial y^3} - A_{22}^{-(0)} \frac{\partial^3 w_s}{\partial y^3} + (A_{12}^{(0)} + A_{66}^{(0)}) \frac{\partial u_0}{\partial x \partial y} \\ & - (A_{12}^{(1)} + 2A_{66}^{(1)}) \frac{\partial^3 w_0}{\partial x \partial y^2} - (A_{12}^{-(0)} + 2A_{66}^{-(0)}) \frac{\partial^3 w_s}{\partial x \partial y^2} \\ & + A_{66}^{(0)} \frac{\partial^3 v_0}{\partial x^2} + \tilde{A}_{13}^{(0)} \frac{\partial \phi}{\partial y} + \bar{B}_{\epsilon 32}^{(0)} \frac{\partial \varphi}{\partial x} + \bar{B}_{\epsilon 32}^{(0)} \frac{\partial \psi}{\partial x} \end{aligned} \right] \\ & = \mathcal{L} \left[m_0\ddot{v}_0 - m_1 \frac{\partial \ddot{w}_0}{\partial y} - m_3 \frac{\partial \ddot{w}_s}{\partial y} \right] \end{aligned} \quad (48b)$$

$$\begin{aligned} \Gamma = & \left[\begin{aligned} & A_{11}^{(1)} \frac{\partial^3 u_0}{\partial x^3} - A_{22}^{(2)} \frac{\partial^4 w_0}{\partial y^4} - A_{11}^{-(1)} \frac{\partial^4 w_s}{\partial y^4} + (A_{12}^{(1)} + 2A_{66}^{(1)}) \\ & \left(\frac{\partial^3 u_0}{\partial x \partial y^2} + \frac{\partial^3 v_0}{\partial x^2 \partial y} \right) - 2(A_{12}^{(2)} + 2A_{66}^{(2)}) \frac{\partial^4 w_0}{\partial x^2 \partial y^2} \\ & - 2(A_{12}^{-(1)} + 2A_{66}^{-(1)}) \frac{\partial^4 w_s}{\partial x^2 \partial y^4} + A_{22}^{(1)} \frac{\partial^3 v_0}{\partial x^3} - A_{22}^{(2)} \frac{\partial^4 w_0}{\partial y^4} \\ & - A_{22}^{-(1)} \frac{\partial^4 w_s}{\partial y^4} + \tilde{A}_{13}^{(1)} \frac{\partial^2 \phi}{\partial x^2} + A_{23}^{(1)} \frac{\partial^2 \phi}{\partial y^2} + \bar{B}_{\epsilon 31}^{-(1)} \frac{\partial^2 \varphi}{\partial x^2} \\ & + \bar{B}_{\epsilon 32}^{(1)} \frac{\partial^2 \varphi}{\partial y^2} + \bar{B}_{q31}^{(1)} \frac{\partial^2 \psi}{\partial x^2} + \bar{B}_{q32}^{(1)} \frac{\partial^2 \psi}{\partial y^2} \end{aligned} \right] \\ & = \mathcal{L} \left[\begin{aligned} & (P_{x0} + P_{\epsilon 31} + P_{q31}) \frac{\partial^2 w_0}{\partial x^2} + (P_{y0} + P_{\epsilon 32} + P_{q32}) \frac{\partial^2 w_0}{\partial y^2} \\ & + m_0(\ddot{w}_0 + \ddot{w}_s) + m_1 \left(\frac{\partial \ddot{u}_0}{\partial x} + \frac{\partial \ddot{v}_0}{\partial y} \right) - m_2 \left(\frac{\partial^2 \ddot{w}_0}{\partial x^2} + \frac{\partial^2 \ddot{w}_0}{\partial y^2} \right) \\ & - m_4 \left(\frac{\partial^2 \ddot{w}_0}{\partial x^2} + \frac{\partial^2 \ddot{w}_0}{\partial y^2} \right) + m_6\ddot{\phi} \end{aligned} \right] \end{aligned} \quad (48c)$$

$$\begin{aligned} \Gamma = & \left[\begin{aligned} & \bar{A}_{11}^{(0)} \frac{\partial^3 u_0}{\partial x^3} - \bar{A}_{11}^{(1)} \frac{\partial^4 w_0}{\partial x^4} - \bar{A}_{11}^{-(f)} \frac{\partial^4 w_s}{\partial x^4} + (\bar{A}_{12}^{(0)} + 2\bar{A}_{66}^{(0)}) \\ & \left(\frac{\partial^3 u_0}{\partial x \partial y} + \frac{\partial^3 v_0}{\partial x^2 \partial y} \right) - 2(\bar{A}_{12}^{(1)} + 2\bar{A}_{66}^{(1)}) \frac{\partial^4 w_0}{\partial x^2 \partial y^2} \\ & - 2(\bar{A}_{12}^{-(f)} + 2\bar{A}_{66}^{-(f)}) \frac{\partial^4 w_s}{\partial x^2 \partial y^2} + \bar{A}_{22}^{(0)} \frac{\partial^3 v_0}{\partial y^3} - \bar{A}_{22}^{(1)} \frac{\partial^4 w_0}{\partial y^4} \\ & - \bar{A}_{22}^{-(f)} \frac{\partial^4 w_s}{\partial y^4} + \hat{A}_{44}^{(0)} \frac{\partial^2 w_s}{\partial y^2} + \hat{A}_{55}^{(0)} \frac{\partial^2 w_s}{\partial x^2} + (\tilde{A}_{13}^{-(f)} + \hat{A}_{55}^{(0)}) \frac{\partial^2 \phi}{\partial x^2} \\ & + (\tilde{A}_{23}^{-(f)} + \hat{A}_{44}^{(0)}) \frac{\partial^2 \phi}{\partial y^2} + \left((B_{\epsilon 31}^{-(f)} - B_{\epsilon 15}^{(g)}) \frac{\partial^2 \phi}{\partial x^2} + \ddot{w}_s \right) \\ & + m_3 \left(\frac{\partial \ddot{u}_0}{\partial x} + \frac{\partial \ddot{v}_0}{\partial y} \right) - m_4 \left(\frac{\partial^2 \ddot{w}_0}{\partial x^2} (\bar{B}_{\epsilon 32}^{-(f)} - \bar{B}_{\epsilon 34}^{(g)}) \frac{\partial^2 \kappa}{\partial y^2} \right) \\ & + (\bar{B}_{q31}^{-(f)} - \bar{B}_{q15}^{(g)}) \frac{\partial^2 \varphi}{\partial x^2} + (\bar{B}_{q32}^{-(f)} - \bar{B}_{q24}^{(g)}) \frac{\partial^2 \psi}{\partial y^2} \end{aligned} \right] \\ & = \mathcal{L} \left[\left(m_0 \left(\ddot{w}_0 + \frac{\partial^2 \ddot{w}_0}{\partial y^2} \right) \right) - m_5 \left(\frac{\partial^2 \ddot{w}_s}{\partial x^2} + \frac{\partial^2 \ddot{w}_s}{\partial y^2} \right) + m_6\ddot{\phi} \right] \end{aligned} \quad (48d)$$

$$\Gamma = \begin{bmatrix} -\tilde{A}_{13}^{(0)} \frac{\partial u_0}{\partial x} + \tilde{A}_{13}^{(1)} \frac{\partial w_0}{\partial x^2} + (-\tilde{A}_{13}^{(f)} + \hat{A}_{55}^{(0)}) \frac{\partial^2 w_s}{\partial x^2} \\ -\tilde{A}_{23}^{(0)} \frac{\partial v_0}{\partial x} + \tilde{A}_{23}^{(1)} \frac{\partial^2 w_0}{\partial y^2} + (-\tilde{A}_{23}^{(f)} + \hat{A}_{44}^{(0)}) \frac{\partial^2 w_s}{\partial y^2} - \tilde{A}_{33}^{(g)} \phi \\ + \hat{A}_{44}^{(0)} \frac{\partial^2 \phi}{\partial y^2} + \hat{A}_{55}^{(0)} \frac{\partial^2 \phi}{\partial x^2} - \bar{B}_{e15}^{(g)} \frac{\partial^2 \phi}{\partial x^2} - \bar{B}_{e24}^{(g)} \frac{\partial^2 \phi}{\partial y^2} - \bar{B}_{q15}^{(g)} \frac{\partial^2 \phi}{\partial x^2} \\ - \bar{B}_{q24}^{(g)} \frac{\partial^2 \psi}{\partial y^2} - \bar{B}_{e33}^{(g)} \phi - \bar{B}_{q33}^{(g)} \psi + \bar{B}_{e33}^{(1)} + \bar{B}_{q33}^{(g)} \end{bmatrix}$$

$$= \mathcal{L} [m_6(\ddot{w}_0 + \ddot{w}_s) + m_7\ddot{\phi}] - \tilde{A}_{13}^{(0)} \frac{\partial u_0}{\partial x} + \tilde{A}_{13}^{(1)} \frac{\partial^2 w_0}{\partial x^2}$$

$$+ (\tilde{A}_{13}^{(f)} + \hat{A}_{55}^{(0)}) \frac{\partial^2 w_0}{\partial x^2} - \tilde{A}_{23}^{(0)} \frac{\partial v_0}{\partial y} + \tilde{A}_{23}^{(1)} \frac{\partial^2 w_0}{\partial y^2}$$

$$+ (\tilde{A}_{23}^{(f)} + \hat{A}_{44}^{(0)}) \frac{\partial^2 w_s}{\partial y^2} - (-\tilde{A}_{23}^{(f)} + \hat{A}_{23}^{(0)}) \frac{\partial^2 w_s}{\partial y^2} - \tilde{A}_{23}^{(g)} \phi$$

$$+ \hat{A}_{44}^{(0)} \frac{\partial^2 \phi}{\partial x^2} - B_{e15}^{(g)} \frac{\partial^2 \phi}{\partial x^2} - B_{e24}^{(g)} \frac{\partial^2 \phi}{\partial y^2} - B_{q15}^{(g)} \frac{\partial^2 \psi}{\partial x^2} - B_{q24}^{(g)} \frac{\partial^2 \psi}{\partial y^2}$$

$$- \bar{B}_{e33}^{(g)} \phi - \bar{B}_{q33}^{(g)} \psi + B_{e33}^{(1)} B_{q33}^{(1)}$$

$$= \mathcal{L} [m_6(\ddot{w}_0 + \ddot{w}_s) + m_7\ddot{\phi}] \quad (48e)$$

$$\bar{B}_{e31}^{(0)} \frac{\partial u_0}{\partial x} + \bar{B}_{e32}^{(0)} \frac{\partial v_0}{\partial x} - \bar{B}_{e31}^{(1)} \frac{\partial^2 w_0}{\partial x^2} - \bar{B}_{e32}^{(1)} \frac{\partial^2 w_0}{\partial y^2}$$

$$+ (B_{e15}^{(g)} - \bar{B}_{e31}^{(f)}) \frac{\partial^2 w_2}{\partial y^2} + \bar{B}_{e32}^{(g)} \phi + B_{e15}^{(g)} \frac{\partial^2 \phi}{\partial x^2} + B_{e24}^{(g)} \frac{\partial^2 \phi}{\partial y^2}$$

$$- P_{e33}^{(s2)} \phi - P_{g33}^{(c2)} \psi + P_{e11}^{(c2)} \frac{\partial^2 \phi}{\partial x^2} + P_{e22}^{(c2)} \frac{\partial^2 \phi}{\partial y^2} + P_{g22}^{(c2)} \frac{\partial^2 \psi}{\partial x^2}$$

$$+ P_{g22}^{(c2)} \frac{\partial^2 \psi}{\partial y^2} - P_{g33}^{(s)} - P_{e33}^{(s)} = 0 \quad (48f)$$

$$\bar{B}_{q31}^{(0)} \frac{\partial u_0}{\partial x} + \bar{B}_{q32}^{(0)} \frac{\partial v_0}{\partial y} - \bar{B}_{q31}^{(1)} \frac{\partial^2 w_0}{\partial x^2} - \bar{B}_{q32}^{(1)} \frac{\partial^2 w_0}{\partial y^2}$$

$$+ (B_{q15}^{(g)} - \bar{B}_{q31}^{(f)}) \frac{\partial^2 w_s}{\partial x^2} + (B_{q32}^{(g)} - \bar{B}_{q32}^{(f)}) \frac{\partial^2 w_s}{\partial y^2} + \bar{B}_{q33}^{(g)} \phi$$

$$+ B_{q15}^{(g)} \frac{\partial^2 \phi}{\partial x^2} + B_{q24}^{(g)} \frac{\partial^2 \phi}{\partial y^2} = -P_{g33}^{(s2)} \phi - P_{\mu33}^{(c2)} \psi + P_{g11}^{(c2)} \frac{\partial^2 \phi}{\partial x^2}$$

$$+ P_{g22}^{(c2)} \frac{\partial^2 \phi}{\partial y^2} + P_{\mu11}^{(c2)} \frac{\partial^2 \psi}{\partial x^2} + P_{\mu22}^{(c2)} \frac{\partial^2 \psi}{\partial y^2} - P_{g33}^{(s)} - P_{\mu33}^{(s)} = 0 \quad (48g)$$

The definitions of the resulting MEE coefficients are provided in Appendix A1–A3.

$$\begin{pmatrix} u_0 \\ v_0 \\ w_0 \\ w_s \\ \phi \\ \varphi \\ \psi \end{pmatrix} = \sum_{m=1}^{\infty} \sum_{n=1}^{\infty} \begin{pmatrix} \bar{u} \cos(\alpha x) \sin(\beta y) e^{i\omega t} \\ \bar{v} \sin(\alpha x) \cos(\beta y) e^{i\omega t} \\ \bar{w}_0 \sin(\alpha x) \sin(\beta y) e^{i\omega t} \\ \bar{w}_s \sin(\alpha x) \sin(\beta y) e^{i\omega t} \\ \bar{\phi} \sin(\alpha x) \sin(\beta y) e^{i\omega t} \\ \bar{\varphi} \sin(\alpha x) \sin(\beta y) e^{i\omega t} \\ \psi \sin(\alpha x) \sin(\beta y) e^{i\omega t} \end{pmatrix}, \quad \alpha = \frac{m\pi}{L_x}, \beta = \frac{n\pi}{L_y} \quad (49)$$

The remaining seven variables, \bar{u} , \bar{v} , \bar{w}_0 , \bar{w}_s , $\bar{\phi}$, $\bar{\varphi}$, and $\bar{\psi}$, respectively, stand for the greatest displacement, electric, and magnetic potential values. Here, it stands for the natural frequency. For ease of use, these seven variables can be represented as vectors.

2.8. Solution Method

The precise analytical solutions of a simply supported (SS) three-layered rectangular nanoplate are obtained in the research using Navier's solution approach. Due to this, the double trigonometric series expansion is used to solve for the seven unknowns as follows.

$$\{\Delta\} = [\bar{u} \quad \bar{v} \quad \bar{w}_0 \quad \bar{w}_s \quad \bar{\phi} \quad \bar{\varphi} \quad \bar{\psi}]^T \quad (50)$$

The governing equations system is ultimately organized in the following format utilizing the stiffness $[K]$ and inertia $[M]$ matrices, as well as the load vector $\{F\}$:

$$\{[K] - \omega_{mn}^2[M]\}\{\Delta\} = \{F\} \quad (51)$$

In addition, the load vector, neglectable in the free vibration and buckling analysis, is as follows.

$$\{F\} = \begin{bmatrix} 0 & 0 & 0 & 0 & -(B_{e33}^{(g)} + B_{q33}^{(g)}) & -(P_{g33}^{(g)} + P_{e33}^{(g)}) & -(P_{g33}^{(g)} + P_{e33}^{(g)}) \end{bmatrix} \quad (52)$$

In the case of free vibration analysis, the nanoplate's governing equation system under in-plane static forces is defined as follows.

$$\{[K] - \omega_{mn}^2[M]\}\{\Delta\} = \{0\} \quad (53)$$

Also, just for nanoplate's buckling analysis, the system of governing equations is

$$[K]\{\Delta\} = \{0\} \quad (54)$$

The elements of symmetric ($K_{ij} = K_{ji}$) stiffness $[K]$ and symmetric ($M_{ij} = M_{ji}$) inertia matrixes are given in the Appendix A4 and A5 section.

2.9. Validation

The following nondimensional frequency parameter (Equation (36)) is defined in the same manner as the researches of ref. [50,51] in order to verify the current investigation. Here, the bottom material's mass density and elasticity modulus are $\rho_b = 5300 \text{ kg m}^{-3}$ and $C_{b11} = 166 \text{ GPa}$, respectively (BaTiO₃). The plate has a rectangular form, $a = 2 \text{ m}$, $b = 1 \text{ m}$, ratio $h/a = 0.2$, and is made of BaTiO₃/CoFe₂O₄ with $p = 1$.

$$\bar{\omega} = \omega_{(m,n)} \left(\frac{a^2}{h} \right) \sqrt{\frac{\rho_b}{C_{b11}}} \quad (55)$$

Table 4 compares the dimensionless frequencies of the current investigation with those of the literature studies. Table 4 shows that, except for the first and second modes, the findings of the recent research and ref. [50] are comparable.

The following tables present a comparison of the three nonlocal plate theories in terms of the maximum deflection and natural frequencies, as determined in another study^[52] The dimensionless maximum deflections obtained from three nonlocal plate theories are compared with the results of the current inquiry in Table 3 and 4. This comparison is based on different

Table 3. Temperature-dependent coefficients for the properties of Si₃N₄ and SUS304.^[36,53]

Material	Property	P_{-1}	P_0	P_1	P_2	P_3	P ($T = 300$ K)
Nickel	E [Pa]	0	$223.95e + 9$	$-2.794e-4$	$3.998e-9$	0	$207.7877e + 9$
	ν	0	0.31	0	0	0	0.31
	α [1 K^{-1}]	0	$9.9209e-6$	$8.705e-4$	0	0	$15.32e-6$
	κ [W m K^{-1}]	0	0	15.397	$-1.264e-3$	$2.09e-6$	$-7.223e-10$
	ρ [kg m^{-3}]	0	8900	0	0	0	8900

Table 4. Comparison of the dimensionless frequencies $\bar{\omega}$ of an FG SS rectangular plate consisting of BaTiO₃/CoFe₂O₄.

Mode	Reference [51]	Reference [50]	Present Study
(1,1)	9.525	10.0244	16.6437
(2,2)	28.762	32.5716	51.9655
(3,3)	50.966	66.2842	77.9483
(4,4)	131.186	104.0065	103.9311
(5,5)	139.106	129.6477	129.9139

nonlocal parameters and thickness values for square and rectangular plates subjected to uniformly distributed and point loads. The assessments revealed that the results of the current investigation were similar to those of studies employing first- and third-order theories. In addition, the nonlocal theory yielded more accurate predictions for larger displacements. Moreover, the results obtained from the first- and third-order theories were approximately the same for all nonlocal effect values. **Table 5** and **6** compare the calculated natural frequencies of the third-order nonlocal plate theories, considering different nonlocal parameters and aspect ratio values. The subsequent formulae were employed to compare the utmost nondimensional deflection and natural frequencies:

$$\bar{w} = -w \left(\frac{Eh^2}{q_0 a^4} \right) 10^2 \quad \bar{w} = -w \left(\frac{Eh^2}{Q_0 a^4} \right) 10^2 \quad \bar{\omega} = \omega h \sqrt{\frac{\rho}{G}} \quad (56)$$

where Q_0 and q_0 denote the size of the point and uniform loads, the parameters a , E , ν , and represent the plate's length, elastic modulus, Poisson's ratio, and density.

Table 5 presents a comparison of the calculated deflections of a supported isotropic plate with specific parameters: $a = 10$, $\nu = 0.3$ for the Poisson ratio, and $E = 300 \times 10^6$ for the elastic modulus. These deflections are the result of applying a single load, $q_0 = 1$ N. **Table 6** presents a comparison of the calculated deflections of a supported, isotropic plate with specific values for its dimensions and material properties. The plate has a length of 10 units, Poisson ratio of 0.3, and an elastic modulus of 300×10^6 units. The deflections are determined by applying a uniform load of 1 N m^{-1} up to a series of 100 terms. The study in **Table 7** compares different hypotheses from the literature with the calculated nondimensional first mode frequency $\bar{\omega}_{11}$ of a supported isotropic plate. The plate has a length of 10 units ($a = 10$), a Poisson ratio of 0.3 ($\nu = 0.3$), and an elasticity modulus of 300×10^6 . The comparison in **Table 8** examines investigations

that utilize different theories from the literature, with the computed nondimensional higher-order frequencies $\bar{\omega}$ of a SS isotropic plate. The plate has specific parameters: $a = 10$, $a/b = 1$, $a/h = 100$, Poisson ratio $\nu = 0.3$, and modulus of elasticity $E = 300 \times 10^6$.

3. Numerical Analysis

This section investigates the change in the mechanical properties of the sandwich smart nanoplate. First, the numerical analyses are performed for the only core auxetic core plate according to an inclined angle to determine some mechanical properties (E_{11}^c , E_{22}^c , G_{12}^c , G_{13}^c , G_{23}^c , ρ^c , ν_{12}^c , ν_{21}^c and α_{11}^c). **Figure 2** shows the effect of the β_1 parameter ($\beta_1 = dd/ll$) upon the elasticity module E_{11}^c of the auxetic core in xx direction according to an inclined angle in the range of $[10^\circ, 80^\circ]$ with the increment step $\Delta\theta = 1^\circ$. The auxetic core material of the smart nanoplate has been determined to be nickel. The core nanoplate parameters as considered are $a = 1e-6$, $dd = a/100$, $tt = a/500$, $ll = a/100$, and $\beta_3 = 0.15$ ($\beta_3 = tt/ll$). As shown in the figure, as the β_1 parameter increases for any inclined fixed value, the elasticity module value of the nanosmart core plate on the xx direction rises too. For example, for the inclined angle $\theta = 60^\circ$, the elasticity module in the direction xx E_{11}^c has been determined as $0.5e10$, $1.2e10$, $1.7e10$, and $2.2e10$ considering four different $\beta_1 = 2$, $\beta_1 = 4$, $\beta_1 = 6$, and $\beta_1 = 8$, respectively. On the other hand, as shown in the figure, with the increase in the inclined angle θ for any β_1 parameter, the elasticity module parameter E_{11}^c in that direction, xx , increases, too. **Figure 3** depicts the influence of the β_1 parameter ($\beta_1 = dd/ll$) on the elastic modulus of the auxetic core in the yy direction (E_{22}^c). The analysis considers an inclined angle ranging from 10° to 80° , with an increment step of 1° . The nickel is designated as the auxetic core material for the smart nanoplate. The core nanoplate characteristics are defined as follows: $a = 1e-6$, $dd = a/100$, $tt = a/500$, $ll = a/100$, and $\beta_3 = 0.15$ ($\beta_3 = tt/ll$). The figure shows that an increase in the β_1 parameter while keeping the inclined angle constant leads to a decrease in the nanosmart core plate's elastic modulus (E_{22}^c) in the yy direction. For example, for the constant inclined angle value $\theta = 30^\circ$, the value of the elasticity module on the direction yy E_{22}^c has been determined as $1.5e9$, $0.68e9$, $0.43e9$, and $0.41e9$ Pa considering $\beta_1 = 2$, $\beta_1 = 4$, $\beta_1 = 6$, $\beta_1 = 8$, respectively. In contrast, the diagram also demonstrates that as the angle of inclination θ increases for any given β_1 parameter, the elastic modulus parameter E_{22}^c in the yy direction decreases correspondingly. This indicates a continuous pattern where an increase in β_1 or the inclined angle θ results in a

Table 5. Comparison of nondimensional maximum center deflection \bar{w} in SS plate under uniform load q_0 ($q_0 = 1$, $a = 10$, $\nu = 0.3$ and $E = 300 \times 10^6$).

a/b	a/h	μ	Classical	First-order ^[52]	Third-order ^[52]	Present (High-order)
1	10	0	4.0083	4.1853	4.1853	4.1854
		0.5	4.3702	4.5608	4.5607	4.5607
		1	4.7322	4.9363	4.9362	4.9362
		1.5	5.0942	5.3118	5.3116	5.3116
		2	5.4561	5.6873	5.6871	5.6879
		2.5	5.8181	6.0628	6.0625	6.0630
	50	0	4.0083	4.0154	4.0154	4.0153
		0.5	4.3702	4.3779	4.3779	4.3781
		1	4.7322	4.7404	4.7404	4.7410
		1.5	5.0942	5.1029	5.1029	5.1033
		2	5.4561	5.4654	5.4654	5.4650
		2.5	5.8181	5.8279	5.8279	5.8280
	100	0	4.0083	4.01	4.01	4.0122
		0.5	4.3702	4.3721	4.3721	4.3725
		1	4.7322	4.7342	4.7342	4.7340
		1.5	5.0942	5.0963	5.0963	5.0960
		2	5.4561	5.4584	5.4584	5.4588
		2.5	5.8181	5.8205	5.8205	5.8208
2	10	0	0.6483	0.717	0.7169	0.7180
		0.5	0.7946	0.8768	0.8767	0.8760
		1	0.9408	1.0366	1.0364	1.0361
		1.5	1.087	1.1965	1.1961	1.1970
		2	1.2332	1.3563	1.3558	1.3560
		2.5	1.3794	1.5161	1.5155	1.5165
	50	0	0.6483	0.6511	0.6511	0.6508
		0.5	0.7946	0.7978	0.7978	0.7985
		1	0.9408	0.9446	0.9446	0.9440
		1.5	1.087	1.0914	1.0914	1.0917
		2	1.2332	1.2381	1.2381	1.2384
		2.5	1.3794	1.3849	1.3849	1.3846
	100	0	0.6483	0.649	0.649	0.6485
		0.5	0.7946	0.7954	0.7954	0.7950
		1	0.9408	0.9417	0.9417	0.9415
		1.5	1.087	1.0881	1.0881	1.0883
		2	1.2332	1.2344	1.2344	1.2340
		2.5	1.3794	1.3808	1.3808	1.3805
3	1.5256	1.5271	1.5271	1.5265		

Table 6. Comparison of the supported plate's nondimensional maximum center deflection w under the central Q_0 point load ($Q_0 = 1$, $a = 10$, $E = 300 \times 10^6$, $\nu = 0.3$, 100 term series).

a/b	a/h	μ	Classical	First-order ^[52]	Third-order ^[52]	Present (High-order)
1	10	0	0.4609	0.5147	0.5137	0.5180
		0.5	0.5752	0.821	0.8072	0.8222
		1	0.6894	1.1274	1.1008	1.1270
		1.5	0.8037	1.4337	1.3944	1.4340
		2	0.918	1.7401	1.688	1.7505
		2.5	1.0322	2.0465	1.9816	2.0484
	50	0	0.4609	0.463	0.463	0.4640
		0.5	0.5752	0.585	0.585	0.5865
		1	0.6894	0.707	0.7069	0.7092
		1.5	0.8037	0.8289	0.8288	0.8285
		2	0.918	0.9509	0.9508	0.9510
		2.5	1.0322	1.0728	1.0727	1.0725
	100	0	0.4609	0.4614	0.4614	0.4611
		0.5	0.5752	0.5776	0.5776	0.5778
		1	0.6894	0.6938	0.6938	0.6935
		1.5	0.8037	0.81	0.81	0.8150
		2	0.918	0.9262	0.9262	0.9260
		2.5	1.0322	1.0424	1.0424	1.0420
2	10	0	0.1685	0.2183	0.2165	0.2188
		0.5	0.2753	0.7092	0.6528	0.7090
		1	0.3821	1.2002	1.089	1.2008
		1.5	0.4889	1.6911	1.5253	1.6907
		2	0.5957	2.182	1.9616	2.1835
		2.5	0.7025	2.6729	2.3979	2.6724
	50	0	0.1685	0.1705	0.1705	0.1700
		0.5	0.2753	0.2927	0.2926	0.2930
		1	0.3821	0.4148	0.4146	0.4152
		1.5	0.4889	0.537	0.5367	0.5394
		2	0.5957	0.6592	0.6587	0.6590
		2.5	0.7025	0.7813	0.7808	0.7816
	100	0	0.1685	0.169	0.169	0.1685
		0.5	0.2753	0.2796	0.2796	0.2791
		1	0.3821	0.3903	0.3903	0.3901
		1.5	0.4889	0.5009	0.5009	0.5010
		2	0.5957	0.6116	0.6115	0.6111
		2.5	0.7025	0.7222	0.7222	0.7225
3	0.8093	0.8328	0.8328	0.8330		

Table 7. Comparison of nondimensional first-mode frequency $\bar{\omega}_{11}$ of SS plate ($a = 10$, $E = 300 \times 10^6$, $\nu = 0.3$).

a/b	a/h	μ	Classical	First-order ^[52]	Third-order ^[52]	Present (High-orde)
1	10	0	0.0963	0.093	0.0935	0.0935
		1	0.088	0.085	0.0854	0.0851
		2	0.0816	0.0788	0.0791	0.0781
		3	0.0763	0.0737	0.0741	0.0732
		4	0.072	0.0696	0.0699	0.0699
	5	0.0683	0.066	0.0663	0.0665	
	20	0	0.0241	0.0239	0.0239	0.0240
		1	0.022	0.0218	0.0218	0.0215
		2	0.0204	0.0202	0.0202	0.0207
		3	0.0191	0.0189	0.0189	0.0190
4		0.018	0.0178	0.0179	0.0175	
2	10	0	0.0602	0.0589	0.0591	0.0590
		1	0.0568	0.0556	0.0557	0.0551
		2	0.0539	0.0527	0.0529	0.0524
		3	0.0514	0.0503	0.0505	0.0501
		4	0.0493	0.0482	0.0483	0.0488
	5	0.0473	0.0463	0.0464	0.0464	
	20	0	0.015	0.015	0.015	0.0152
		1	0.0142	0.0141	0.0141	0.0140
		2	0.0135	0.0134	0.0134	0.0135
		3	0.0129	0.0128	0.0128	0.0130
4		0.0123	0.0123	0.0123	0.0120	
5	0.0118	0.0118	0.0118	0.0116		

decrease in the elastic modulus of the nanosmart core plate in the yy direction.

Figure 4 exhibits the effect of the β_1 parameter ($\beta_1 = dd/ll$) on the shear modulus (G_{12}^c) of the auxetic core in the xy plane. The analysis encompasses an inclined angle spanning from 10° to 80° , with a step size 1° . The smart nanoplate's auxetic core is made of nickel. The fundamental properties of the nanoplate can be described as follows: $a = 1e-6$, $dd = a/100$, $tt = a/500$, $ll = a/100$, and $\beta_3 = 0.15$ (where β_3 is defined as tt/ll). The graph illustrates that an augmentation in the β_1 parameter, with the constant inclined angle, leads to a decrease in the shear modulus (G_{12}^c) of the nanosmart core plate in the xy plane. For example, for the constant inclined angle $\theta = 70^\circ$, the shear module of the auxetic core on the xy plate has been determined as $2e8$, $0.6e8$, $0.28e8$, and $0.19e8$ Pa, considering $\beta_1 = 2$, $\beta_1 = 4$, $\beta_1 = 6$, $\beta_1 = 8$ respectively. In contrast, the figure also demonstrates that as the inclination angle (θ) grows for a given β_1 parameter, the shear modulus parameter G_{12}^c in the xy plane likewise increases. But it is clearly seen that considering a small inclined angle value such as in the range of $[10^\circ, 40^\circ]$, the slope of the curve is small and the curve is almost parallel to the x -axis. On the other hand, as the inclination angle increases, the slope of the curve increases, too, especially in the range of $[40-80^\circ]$. This indicates a consistent pattern in which an increase in β_1 or the inclined

Table 8. Comparison of nondimensional higher-order frequencies ($\bar{\omega}$) of SS plate ($a = 10$, $a/b = 1$, $a/h = 100$, $E = 300 \times 10^6$, $\nu = 0.3$).

Frequencies	μ	Classical	First-order ^[52]	Third-order ^[52]	Present (High-order)
ω_{11}	0	0.0963	0.093	0.0935	0.0932
	1	0.088	0.085	0.0854	0.0851
	2	0.0816	0.0788	0.0791	0.0785
	3	0.0763	0.0737	0.0741	0.0739
	4	0.072	0.0696	0.0699	0.0699
ω_{22}	0	0.3853	0.3414	0.3458	0.3410
	1	0.288	0.2552	0.2585	0.2555
	2	0.2399	0.2126	0.2153	0.2129
	3	0.2099	0.186	0.1884	0.1862
	4	0.1889	0.1674	0.1696	0.1677
ω_{33}	0	0.8669	0.6889	0.702	0.6890
	1	0.5202	0.4134	0.4213	0.4132
	2	0.4063	0.3228	0.329	0.3230
	3	0.3446	0.2738	0.279	0.2735
	4	0.3045	0.242	0.2466	0.2422
5	0.2757	0.2191	0.2233	0.2194	

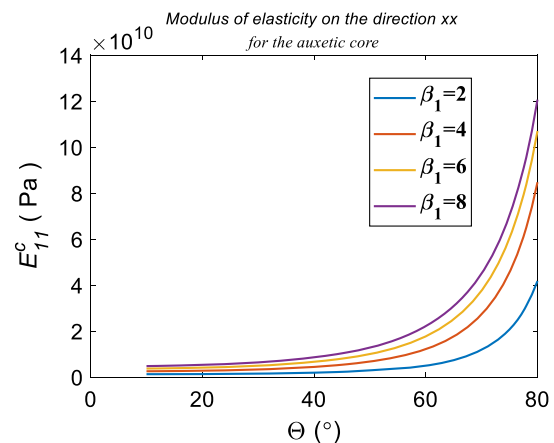


Figure 2. Comparison of the elasticity module of the auxetic core nano plate depending on the four different β_1 parameter values ($\beta_1 = 2$, $\beta_1 = 4$, $\beta_1 = 6$, $\beta_1 = 8$), $\beta_3 = 0.15$, inclined angle θ with the range of $[10^\circ, 80^\circ]$ with the increment step $\Delta\theta = 1^\circ$ on the direction xx . The auxetic core material of the smart nanoplate has been determined to be nickel. The core nano plate parameters as considered $a = 1e-6$, $dd = a/100$, $tt = a/500$, $ll = a/100$.

angle θ results in an enhancement in the shear modulus of the nanosmart core plate in the xy plane. Furthermore, it is essential to mention that when the θ value remains constant, an elevation in the β_1 parameter results in a reduction in G_{12}^c , highlighting the reciprocal correlation between β_1 and G_{12}^c for a fixed inclination angle.

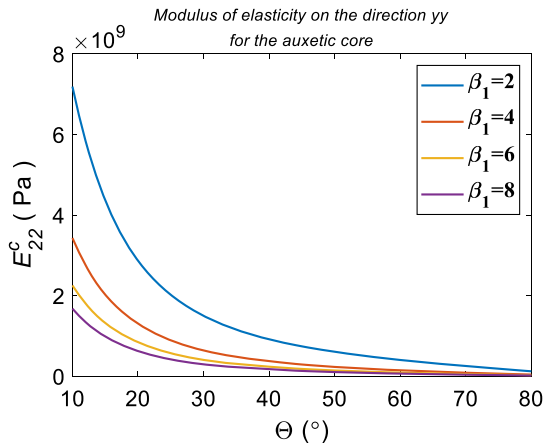


Figure 3. Comparison of the elasticity module of the auxetic core nano plate depending on the four different β_1 parameter values ($\beta_1 = 2, \beta_1 = 4, \beta_1 = 6, \beta_1 = 8$), $\beta_3 = 0.15$, inclined angle θ with the range of $[10^\circ, 80^\circ]$ with the increment step $\Delta\theta = 1^\circ$ on the direction yy . The auxetic core material of the smart nanoplate has been determined to be nickel. The core nano plate parameters as considered $a = 1e-6$, $dd = a/100$, $tt = a/500$, $ll = a/100$.

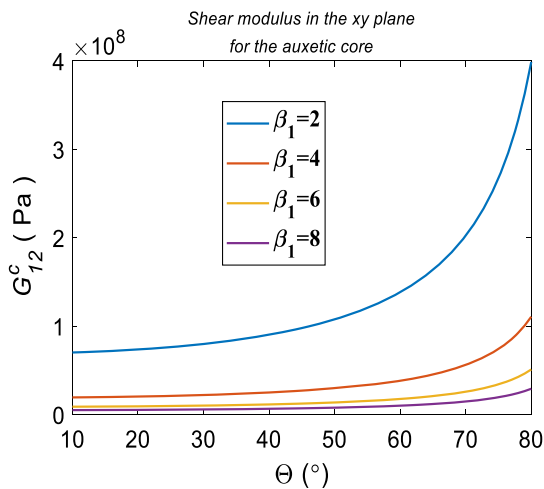


Figure 4. Comparison of the shear module of the auxetic core nano plate depending on the four different β_1 parameter values ($\beta_1 = 2, \beta_1 = 4, \beta_1 = 6, \beta_1 = 8$), $\beta_3 = 0.15$, inclined angle θ with the range of $[10^\circ, 80^\circ]$ with the increment step $\Delta\theta = 1^\circ$ on the xy plane. The auxetic core material of the smart nanoplate has been determined to be nickel. The core nano plate parameters as considered $a = 1e-6$, $dd = a/100$, $tt = a/500$, $ll = a/100$.

Figure 5 illustrates the impact of the β_1 parameter ($\beta_1 = dd/ll$) on the tensile modulus (G_{13}^c) of the auxetic core in the xz plane. The analysis covers an inclination angle that varies from 10° to 80° , with an increment of 1° . The smart nanoplate's auxetic core is made of nickel. The essential characteristics of the nanoplate can be delineated as follows. The values are as follows: $a = 1e-6$, $dd = a/100$, $tt = a/500$, $ll = a/100$, and $\beta_3 = 0.15$ (where β_3 is defined as tt/ll). The graph demonstrates that an increase in the β_1 parameter, while the inclined angle is constant, leads to a rise in the tensile modulus (G_{13}^c) of the nanosmart core plate

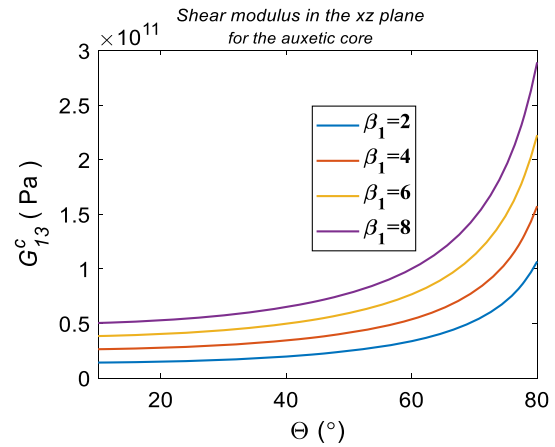


Figure 5. Comparison of the shear module of the auxetic core nano plate depending on the four different β_1 parameter values ($\beta_1 = 2, \beta_1 = 4, \beta_1 = 6, \beta_1 = 8$), $\beta_3 = 0.15$, inclined angle θ with the range of $[10^\circ, 80^\circ]$ with the increment step $\Delta\theta = 1^\circ$ on the direction xz . The auxetic core material of the smart nanoplate has been determined to be nickel. The core nano plate parameters as considered $a = 1e-6$, $dd = a/100$, $tt = a/500$, $ll = a/100$.

in the yz plane. For example, for the constant inclined angle $\theta = 70^\circ$, the shear module of the auxetic core on the xz plate has been determined as $0.49e8, 0.72e8, 0.98e8$, and $1.2e8$ Pa considering $\beta_1 = 2, \beta_1 = 4, \beta_1 = 6, \beta_1 = 8$, respectively. In contrast, the picture clearly shows that as the inclination angle (θ) increases for a given β_1 parameter, the tensile modulus parameter G_{13}^c in the xz plane similarly increases. This indicates a consistent correlation where an increase in β_1 or the inclined angle θ improves the tensile modulus of the nanosmart core plate in the xz plane. However, it is seen that considering small inclined angle values such as in the range of $[10^\circ, 40^\circ]$, the slope of the curve is small, and the curve is almost parallel to the x -axis. On the other hand, as the inclination angle increases, the slope of the curve increases, too, especially in the range of $[40-80^\circ]$.

Moreover, **Figure 6** shows the change on the parameter G_{23}^c (the shear module on the yz plane) depending on the inclined angle θ according to four different β_1 parameters ($\beta_1 = 2, \beta_1 = 4, \beta_1 = 6, \beta_1 = 8$). The figure shows the nonlinear relationship between the θ parameter and the shear module. As the angle value is increased up to a specific threshold, the shear modulus also increases. However, beyond this threshold, further increases in the angle value result in a fall in the shear modulus. For instance, when β_1 is equal to 2, every increase in θ within the range of $10-30^\circ$ results in a nonlinear rise in the shear modulus G_{23}^c from $6.3e9$ to $6.7e9$ Pa. However, when $\beta_1 = 2$, any increase in θ within the range of $30-80^\circ$ leads to a nonlinear decrease in the shear modulus G_{23}^c , from $6.7e9$ to $2e9$ Pa. On the other hand, for a constant θ value, increasing the β_1 value causes the shear modulus to decrease. For example, the shear module G_{23}^c values have been observed as $6.7e9, 2.9e9, 1.8e9$, and $1.3e9$ Pa for $\beta_1 = 2, \beta_1 = 4, \beta_1 = 6, \beta_1 = 8$ considering $\theta = 30^\circ$ respectively. On the other hand, it is seen that the slope of the curve is bigger than the small β_1 than the slope of the curve for the small β_1 parameter.

Figure 7 illustrates the influence of the β_1 parameter ($\beta_1 = dd/ll$) on material density ρ^c , considering an inclined angle

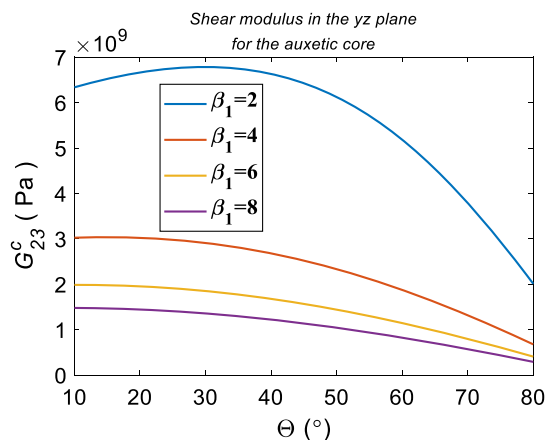


Figure 6. Comparison of the shear module of the auxetic core nano plate depending on the four different β_1 parameter values ($\beta_1 = 2, \beta_1 = 4, \beta_1 = 6, \beta_1 = 8$), $\beta_3 = 0.15$, inclined angle θ with the range of $[10^\circ, 80^\circ]$ with the increment step $\Delta\theta = 1^\circ$ on the direction yz. The auxetic core material of the smart nanoplate has been determined to be nickel. The core nano plate parameters as considered $a = 1e-6$, $dd = a/100$, $tt = a/500$, $ll = a/100$.

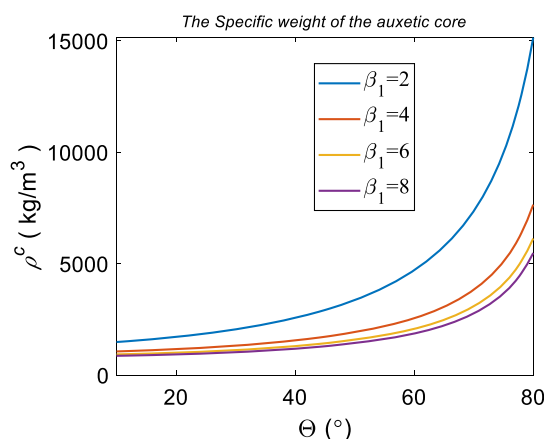


Figure 7. Comparison of the material density (ρ^c) of the auxetic core nano plate depending on the four different β_1 parameter values ($\beta_1 = 2, \beta_1 = 4, \beta_1 = 6, \beta_1 = 8$), $\beta_3 = 0.15$, inclined angle θ with the range of $[10^\circ, 80^\circ]$ with the increment step $\Delta\theta = 1^\circ$. The auxetic core material of the smart nanoplate has been determined to be nickel. The core nano plate parameters as considered $a = 1e-6$, $dd = a/100$, $tt = a/500$, $ll = a/100$.

(θ) that varies from 10° to 80° with a step size of 1° . The investigated intelligent material features a nickel core. The essential characteristics of the material are defined as follows. The values are as follows: $a = 1e-6$, $dd = a/100$, $tt = a/500$, $ll = a/100$, and $\beta_3 = 0.15$ (where β_3 is defined as tt/ll). The figure demonstrates that increasing the β_1 parameter while keeping the inclination angle constant reduces material density (ρ^c). For example, the material density (ρ^c) value of the auxetic core has been obtained as 6986, 3826, 3085, and 2785 kg m^{-3} considering $\beta_1 = 2, \beta_1 = 4, \beta_1 = 6, \beta_1 = 8$, and $\theta = 70^\circ$, respectively. In contrast, the figure also illustrates that as the inclination angle (θ) increases for a fixed β_1 parameter, the material density ρ similarly increases. This indicates a regular trend in which an increase in β_1 or

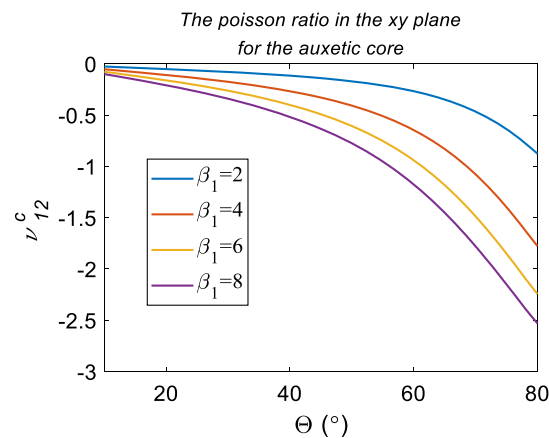


Figure 8. Comparison of the Poisson's ratio ν_{12}^c in the xy direction of the auxetic core nano plate depending on the four different β_1 parameter values ($\beta_1 = 2, \beta_1 = 4, \beta_1 = 6, \beta_1 = 8$), $\beta_3 = 0.15$, inclined angle θ with the range of $[10^\circ, 80^\circ]$ with the increment step $\Delta\theta = 1^\circ$. The auxetic core material of the smart nanoplate has been determined to be nickel. The core nano plate parameters as considered $a = 1e-6$, $dd = a/100$, $tt = a/500$, $ll = a/100$.

the angle θ results in an improvement in material density. Moreover, it is crucial to observe that when the θ value remains consistent, an increase in the β_1 parameter results in a decrease in ρ , emphasizing the inverse relationship between β_1 and material density for a fixed inclination angle.

Figure 8 illustrates the impact of the β_1 parameter on the Poisson's ratio in the xy direction, which is represented as ν_{12}^c . The analysis covers an inclined angle (θ) that varies from 10° to 80° , with a step size of 1° . The essential characteristics of the material are defined as follows. The values are as follows: $a = 1e-6$, $dd = a/100$, $tt = a/500$, $ll = a/100$, and $\beta_3 = 0.15$ (where β_3 is defined as tt/ll). The figure shows that increasing the β_1 parameter while keeping the inclined angle θ constant results in a proportional increase in the Poisson's ratio ν_{12}^c of the nanosmart core plate in the xy direction. In contrast, the image illustrates that as the inclination angle (θ) rises for a given (β_1) parameter, the Poisson's ratio (ν_{12}^c) in the xy plane likewise increases. For example, the Poisson ratio value ν_{12}^c has been obtained as $-2.67, -6.46, -9.4$, and -11.7 , considering $\beta_1 = 2, \beta_1 = 4, \beta_1 = 6, \beta_1 = 8$, and $\theta = 60^\circ$ respectively. The observed consistent pattern suggests that an increase in either (β_1) or the inclined angle (θ) leads to an improvement in the Poisson's ratio of the nanosmart core plate in the xy direction. On the other hand, it is clearly seen that in the figure, the slope of the graph is nearly parallel to x axes in the range of θ $10-40^\circ$. But after that, the inclined angle value is bigger than $\theta = 40^\circ$; as the θ value increases, the slope of the graph increases too.

The analysis of the influence of the β_1 parameter on Poisson's ratio may also be applied to ν_{21}^c , which denotes the Poisson's ratio in the yx direction (**Figure 9**). As the angle of inclination (θ) increases, the value of ν_{21}^c decreases. In addition, when the θ value remains constant, a rise in the β_1 parameter leads to a decrease in the Poisson's ratio in the yx direction. This finding provides academic value by demonstrating a negative correlation between β_1 and Poisson's ratio at a constant inclination angle. In addition, the commentary may emphasize that the pattern

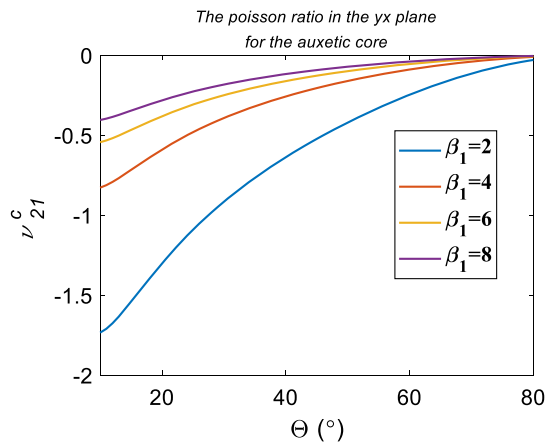


Figure 9. Comparison of Poisson's ratio ν_{21}^c in the yx direction of the auxetic core nano plate depending on the four different β_1 parameter values ($\beta_1 = 2, \beta_1 = 4, \beta_1 = 6, \beta_1 = 8$), $\beta_3 = 0.15$, inclined angle θ with the range of $[10^\circ, 80^\circ]$ with the increment step $\Delta\theta = 1^\circ$. The auxetic core material of the smart nanoplate has been determined to be nickel. The core nano plate parameters as considered $a = 1e-6$, $dd = a/100$, $tt = a/500$, $ll = a/100$.

depicted in the graph does not align with the observed behavior of ν_{12}^c in the xy direction. The presence of parallelism to the x -axis in the θ range of $40-80^\circ$, followed by an increase in slope with θ in the range of $10-40^\circ$, suggests a comparable pattern in both Poisson's ratios. This study confirms that changes in either β_1 or the inclination angle (θ) consistently impact the Poisson's ratio of the nanosmart core plate, particularly in the yx direction (ν_{21}^c).

Figure 10 depicts the influence of the β_1 parameter ($\beta_1 = dd/ll$) on the thermal expansion coefficient (α_{11}^c) in the xx direction. The investigation covers an angular range of $10-80^\circ$, with a 1° increment. The auxetic core of the smart nanoplate, composed of nickel, exhibits the following fundamental properties: $a = 1e-6$, $dd = a/100$, $tt = a/500$, $ll = a/100$, and $\beta_3 = 0.15$

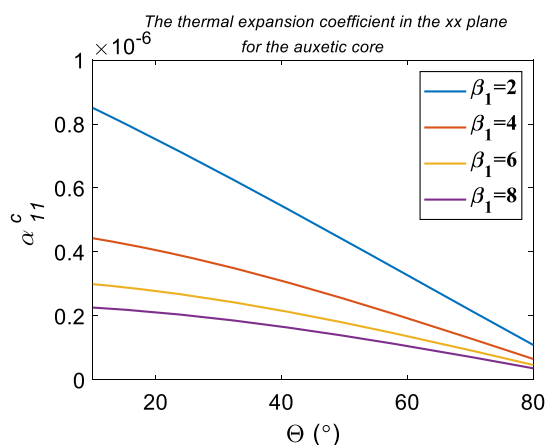


Figure 10. Comparison of thermal expansion coefficient (α_{11}^c) in the xx direction of the auxetic core nano plate depending on the four different β_1 parameter values ($\beta_1 = 2, \beta_1 = 4, \beta_1 = 6, \beta_1 = 8$), $\beta_3 = 0.15$, inclined angle θ with the range of $[10^\circ, 80^\circ]$ with the increment step $\Delta\theta = 1^\circ$. The auxetic core material of the smart nanoplate has been determined to be nickel. The core nano plate parameters as considered $a = 1e-6$, $dd = a/100$, $tt = a/500$, $ll = a/100$.

(where β_3 is defined as tt/ll). The figure reveals that an increase in the β_1 parameter, with the angle of inclination constant, results in a decrease in the thermal expansion coefficient (α_{11}^c) of the nanosmart core plate in the xx direction. Conversely, the figure illustrates that as the inclination angle (θ) increases for a given β_1 parameter, the thermal expansion coefficient α_{11}^c in the xx direction also decreases. This implies a consistent trend where an increase in β_1 or the inclination angle θ leads to a reduction in the thermal expansion coefficient of the nanosmart core plate in the xx direction. It is crucial to note that when the θ value remains constant, an elevation in the β_1 parameter leads to a decrease in α_{11}^c , underscoring the inverse relationship between β_1 and α_{11}^c for a constant inclination angle. On the other hand, as shown in the graph, for small β_1 values, the graph decreases linearly, while for large β_1 values, the graph changes nonlinearly.

Figure 11 illustrates the impact of the β_1 parameter ($\beta_1 = dd/ll$) on the thermal expansion coefficient (α_{22}^c) in the yy direction. The inquiry encompasses a range of angles from 10° to 80° , with a precise increment of 1° . The smart nanoplate's auxetic core, made of nickel, possesses the following essential characteristics: $a = 1e-6$, $dd = a/100$, $tt = a/500$, $ll = a/100$, and $\beta_3 = 0.15$ (where β_3 is defined as tt/ll). As shown in the figure, the change of the thermal expansion coefficient on the yy direction α_{22}^c is very close to each other for all β_1 values according to inclination angle θ .

Figure 12 shows the change of the dimensionless first frequency parameters of the auxetic core sandwich nanosmart plate according to thermal temperature rise ΔT in the range of $0-700^\circ C$ with the increment $10^\circ C$ considering four different β_1 parameters ($\beta_1 = 2.5, \beta_1 = 5, \beta_1 = 7.5, \beta_1 = 10$) $\beta_3 = 0.4$. In this analysis, the inclined angle of the auxetic core $\theta = 45^\circ$, the smart nanoplate's auxetic core is made of nickel, and face plates are made of barium (Br) and cobalt ferrite. The barium and cobalt

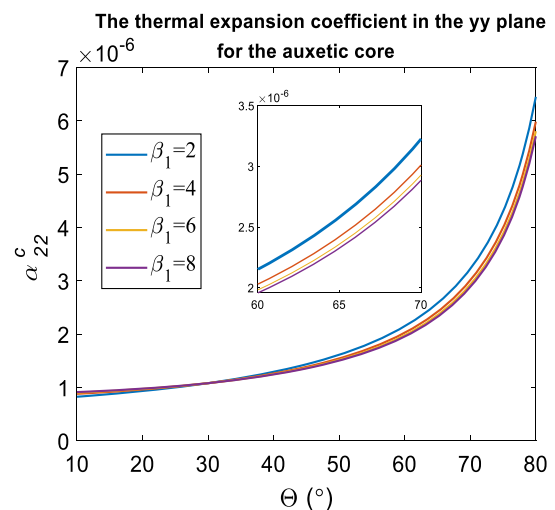


Figure 11. Comparison of thermal expansion coefficient (α_{22}^c) in the yy direction of the auxetic core nano plate depending on the four different β_1 parameter values ($\beta_1 = 2, \beta_1 = 4, \beta_1 = 6, \beta_1 = 8$), $\beta_3 = 0.15$, inclined angle θ with the range of $[10^\circ, 80^\circ]$ with the increment step $\Delta\theta = 1^\circ$. The auxetic core material of the smart nanoplate has been determined to be nickel. The core nano plate parameters as considered $a = 1e-6$, $dd = a/100$, $tt = a/500$, $ll = a/100$.

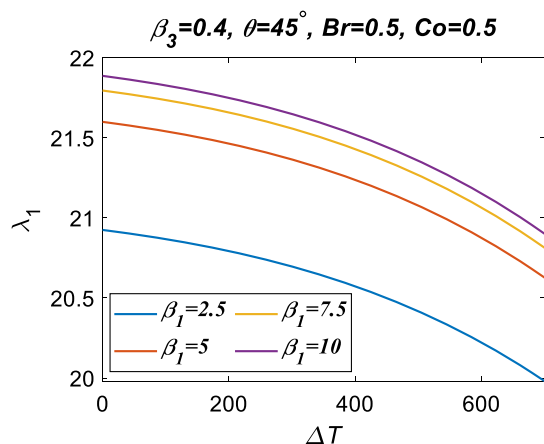


Figure 12. Comparison of dimensionless frequencies λ_1 of the auxetic core nano plate depending on the four different β_1 parameter values ($\beta_1 = 2.5, \beta_1 = 5, \beta_1 = 7.5, \beta_1 = 10$), $\beta_3 = 0.4$, $Br = 0.5$, $Co = 0.5$, NLTR ΔT with the range of $[0^\circ\text{C}, 700^\circ\text{C}]$. The auxetic core material of the smart nanoplate has been determined to be nickel. The core nano plate parameters as considered $a = 1e-6$, $dd = a/100$, $tt = a/500$, $ll = a/100$.

ferrite material ratios are defined as $Br = 0.5$ and $Co = 0.5$. The fundamental properties of the nanoplate can be described as follows: $a = 1e-6$, $b = a$, $hh = a/25$, $hc = hh/5$, $ht = hh/10$, $hp = 0.35 \times hh$, $dd = a/100$, $tt = a/500$, $ll = a/100$, and $\beta_3 = 0.15$ (where β_3 is defined as tt/ll). As shown in the figure, as the NLTR ΔT increases, the dimensionless first frequency parameter of the auxetic core sandwich smart nanoplate decreases gradually. For example, for the parameter $\beta_1 = 2.5$, the dimensionless first frequency parameter has been defined as 20.92 and 19.98 for the NLTR ΔT 0 and 700 °C, respectively. On the other hand, it is seen that in the figure, as the parameter β_1 increases for any NLTR ΔT , the dimensionless first frequency parameter λ_1 increases too. For example, for the temperature rise $\Delta T = 200^\circ\text{C}$, the dimensionless first frequency parameter λ_1 has been derived as 20.79, 21.46, 21.65, and 21.74, respectively.

Figure 13 shows the change of the dimensionless first frequency parameters of the auxetic core sandwich nanosmart plate according to thermal temperature rise ΔT in the range of $0^\circ\text{C} - 700^\circ\text{C}$ with the increment 10°C considering four different β_3 parameters ($\beta_3 = 2.5, \beta_3 = 5, \beta_3 = 7.5, \beta_3 = 10$) $\beta_1 = 2$. In this analysis, the inclined angle of the auxetic core $\theta = 45^\circ$, the smart nanoplate's auxetic core is made of nickel, and face plates are made of barium (Br) and cobalt ferrite (Co). The barium and cobalt ferrite material ratios are defined as $Br = 0.5$ and $Co = 0.5$. The fundamental properties of the nanoplate can be described as follows: $a = 1e-6$, $b = a$, $hh = a/25$, $hc = hh/5$, $ht = hh/10$, $hp = 0.35 \times hh$, $dd = a/100$, $tt = a/500$, $ll = a/100$, and $\beta_3 = 0.15$ (where β_3 is defined as tt/ll). As shown in the figure, as the NLTR ΔT increases, the dimensionless first frequency parameter of the auxetic core sandwich smart nanoplate decreases slightly. For example, for the parameter $\beta_3 = 2.5$, the dimensionless first frequency parameter has been defined as 14.26 and 13.6 for the NLTR ΔT 0 and 700 °C, respectively. On the other hand, it is seen that in the figure, as the increases parameter β_3 for any NLTR ΔT , the dimensionless first frequency parameter λ_1 decreases. For example, for the temperature rise

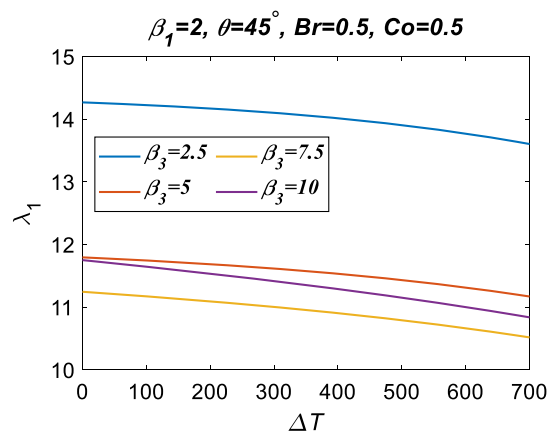


Figure 13. Comparison of dimensionless frequencies λ_1 of the auxetic core nano plate depending on the four different β_3 parameter values ($\beta_3 = 2.5, \beta_3 = 5, \beta_3 = 7.5, \beta_3 = 10$), $\beta_1 = 2$, $Br = 0.5$, $Co = 0.5$, NLTR ΔT with the range of $[0, 700^\circ\text{C}]$. The auxetic core material of the smart nanoplate has been determined to be nickel. The core nano plate parameters as considered $a = 1e-6$, $dd = a/100$, $tt = a/500$, $ll = a/100$.

$\Delta T = 200^\circ\text{C}$, the dimensionless first frequency parameter λ_1 has been derived as 14.16, 11.68, 1.53, and 1, respectively.

Figure 14 shows the change of the dimensionless first frequency parameters of the auxetic core sandwich nanosmart plate according to thermal temperature rise ΔT in the range of $0 - 700^\circ\text{C}$ with the increment 10°C considering four different face plate material Br compound ratio ($Br = 0, Br = 0.33, Br = 0.66, Br = 1$). In this analysis, the inclined angle of the auxetic core $\theta = 45^\circ$, the parameter $\beta_1 = 2, \beta_3 = 0.1$, the smart nanoplate's auxetic core is made of nickel, and face plates are made of barium (Br) and cobalt ferrite (Co). The cobalt material compound of the face plate has been defined with the $Co = 1 - Br$. The fundamental properties of the nanoplate can be described

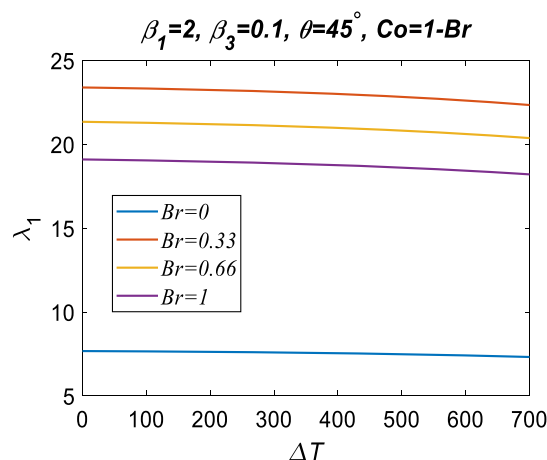


Figure 14. Comparison of dimensionless frequencies λ_1 of the auxetic core nano plate depending on the four different face plate material compound parameters ($Br = 0, Br = 0.33, Br = 0.66, Br = 1$), $\beta_1 = 2, \beta_3 = 0.1, Br = 0.5, Co = 1 - Co$, NLTR ΔT with the range of $[0, 700^\circ\text{C}]$. The auxetic core material of the smart nanoplate has been determined to be nickel. The core nano plate parameters as considered $a = 1e-6$, $dd = a/100$, $tt = a/500$, $ll = a/100$.

as follows: $a = 1e-6$, $b = a$, $hh = a/25$, $h_c = hh/5$, $h_r = hh/10$, $h_p = 0.35 \times hh$, $dd = a/100$, $tt = a/500$, $ll = a/100$, and $\beta_3 = 0.15$ (where β_3 is defined as tt/ll). As shown in the figure, as the NLTR ΔT increases, the dimensionless first frequency parameter of the auxetic core sandwich smart nanoplate decreases slightly. For example, for the parameter $Br = 1$, the dimensionless first frequency parameter has been defined as 19.09 and 18.2 for the NLTR ΔT 0 and 700 °C, respectively. As shown, a decrease of 4% occurred in the decline of the first dimensionless frequency of the plate. On the other hand, in the figure, there is no linear relationship between increasing the Br material ratio of the face plates and the first dimensionless frequency of the smart plate. For example, for the temperature rise $\Delta T = 200$ °C, the dimensionless first frequency parameter λ_1 has been derived as 7.62, 23.24, 21.20, and 18.96, considering $Br = 0$, $Br = 0.33$, $Br = 0.66$, $Br = 1$ respectively.

Figure 15 shows the change of the dimensionless first frequency parameters of the auxetic core sandwich nanosmart plate according to thermal temperature rise ΔT in the range of 0–700 °C with the increment 10 °C considering four different external magnetic potentials ($H_0 = 0$, $H_0 = 1e3$, $H_0 = 3e3$, $H_0 = 5e3$). In this analysis, the inclined angle of the auxetic core $\theta = 45^\circ$, the parameter $\beta_1 = 2$, $\beta_3 = 0.1$, (where β_3 is defined as tt/ll), the smart nanoplate's auxetic core is made of nickel, and face plates are made of barium (Br) and cobalt ferrite (Co). The cobalt material compound of the face plate has been defined with the $Co = 1$ and $Br = 0$. The fundamental properties of the nanoplate can be described as follows: $a = 1e-6$, $b = a$, $hh = a/25$, $h_c = hh/5$, $h_r = hh/10$, $h_p = 0.35 \times hh$, $dd = a/100$, $tt = a/500$, $ll = a/100$. As shown in the figure, as the NLTR ΔT increases, the dimensionless first frequency parameter of the auxetic core sandwich smart nanoplate decreases slightly. For example, for the parameter $H_0 = 0$, the dimensionless first frequency parameter has been defined as 7.67 and 7.31 for the NLTR $\Delta T = 0$ °C and 700 °C, respectively. As shown, a decrease

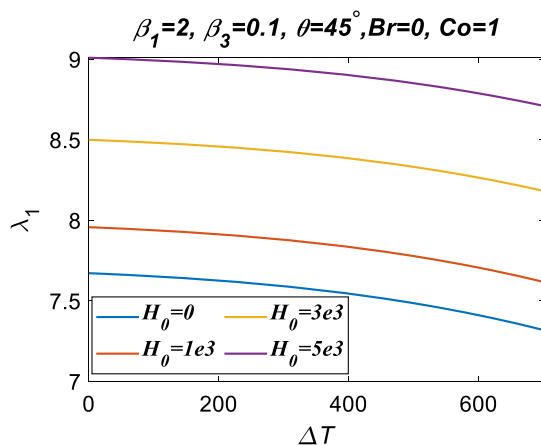


Figure 15. Comparison of dimensionless frequencies λ_1 of the auxetic core nano plate depending on the four different external magnetic potential values ($H_0 = 0$, $H_0 = 1e3$, $H_0 = 3e3$, $H_0 = 5e3$), $\beta_1 = 2$, $\beta_3 = 0.1$, $Br = 0$, $Co = 1$, NLTR ΔT with the range of [0 °C, 700 °C]. The auxetic core material of the smart nanoplate has been determined to be nickel. The core nano plate parameters as considered $a = 1e-6$, $dd = a/100$, $tt = a/500$, $ll = a/100$.

of 4.69% occurred in the decline of the first dimensionless frequency of the plate. On the other hand, in the figure, as the external magnetic potential value increases for any inclined angle θ , the dimensionless first frequency of the auxetic core sandwich smart nanoplate increases, too. For example, for the temperature rise $\Delta T = 200$ °C, the dimensionless first frequency parameter λ_1 has been derived as 7.62, 7.91, 8.45, and 8.96, considering $H_0 = 0$, $H_0 = 1e3$, $H_0 = 3e3$, $H_0 = 5e3$ respectively.

Figure 16 shows the change of the dimensionless first frequency parameters of the auxetic core sandwich nanosmart plate according to thermal temperature rise ΔT in the range of 0–700 °C with the increment 10 °C considering four different external electric potentials ($V_0 = 0$, $V_0 = 1e5$, $V_0 = 5e5$, $V_0 = 1e6$). In this analysis, the inclined angle of the auxetic core $\theta = 45^\circ$, the parameter $\beta_1 = 2$, $\beta_3 = 0.1$, (where β_3 is defined as tt/ll), the smart nanoplate's auxetic core is made of nickel, and face plates are made of barium (Br) and cobalt ferrite (Co). The cobalt material compound of the face plate has been defined with $Co = 0$ and $Br = 1$. The fundamental properties of the nanoplate can be described as follows: $a = 1e-6$, $b = a$, $hh = a/25$, $h_c = hh/5$, $h_r = hh/10$, $h_p = 0.35 \times hh$, $dd = a/100$, $tt = a/500$, $ll = a/100$. As shown in the figure, as the NLTR ΔT increases, the dimensionless first frequency parameter of the auxetic core sandwich smart nanoplate decreases nonlinearly. For example, for the parameter $V_0 = 0$, the dimensionless first frequency parameter has been defined as 19.09 and 18.2 for the NLTR ΔT 0 and 700 °C, respectively.

As shown, a decrease of 4.66% occurred in the decline of the first dimensionless frequency of the plate. On the other hand, in the figure, as the external electric potential value increases for any inclined angle θ , the dimensionless first frequency of the auxetic core sandwich smart nanoplate increases, too. For example, for the temperature rise $\Delta T = 200$ °C, the dimensionless first frequency parameter λ_1 has been derived as 18.96, 19.06, 19.44, and 19.88, considering $V_0 = 0$, $V_0 = 1e5$, $V_0 = 5e5$, and $V_0 = 1e6$, respectively.

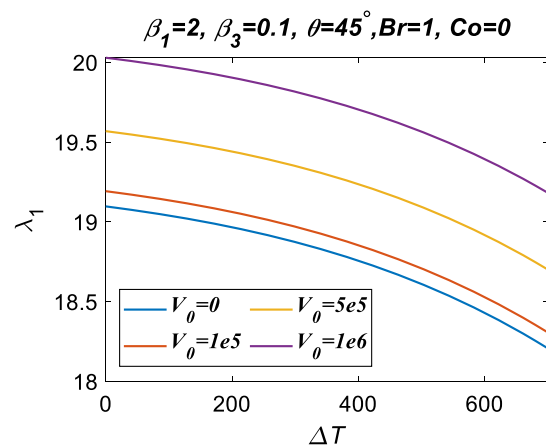


Figure 16. Comparison of dimensionless frequencies λ_1 of the auxetic core nano plate depending on the four different external electric potential values ($V_0 = 0$, $V_0 = 1e5$, $V_0 = 5e5$, $V_0 = 1e6$), $\beta_1 = 2$, $\beta_3 = 0.1$, $Br = 0$, $Co = 1$, NLTR ΔT with the range of [0, 700 °C]. The auxetic core material of the smart nanoplate has been determined to be nickel. The core nano plate parameters as considered $a = 1e-6$, $dd = a/100$, $tt = a/500$, $ll = a/100$.

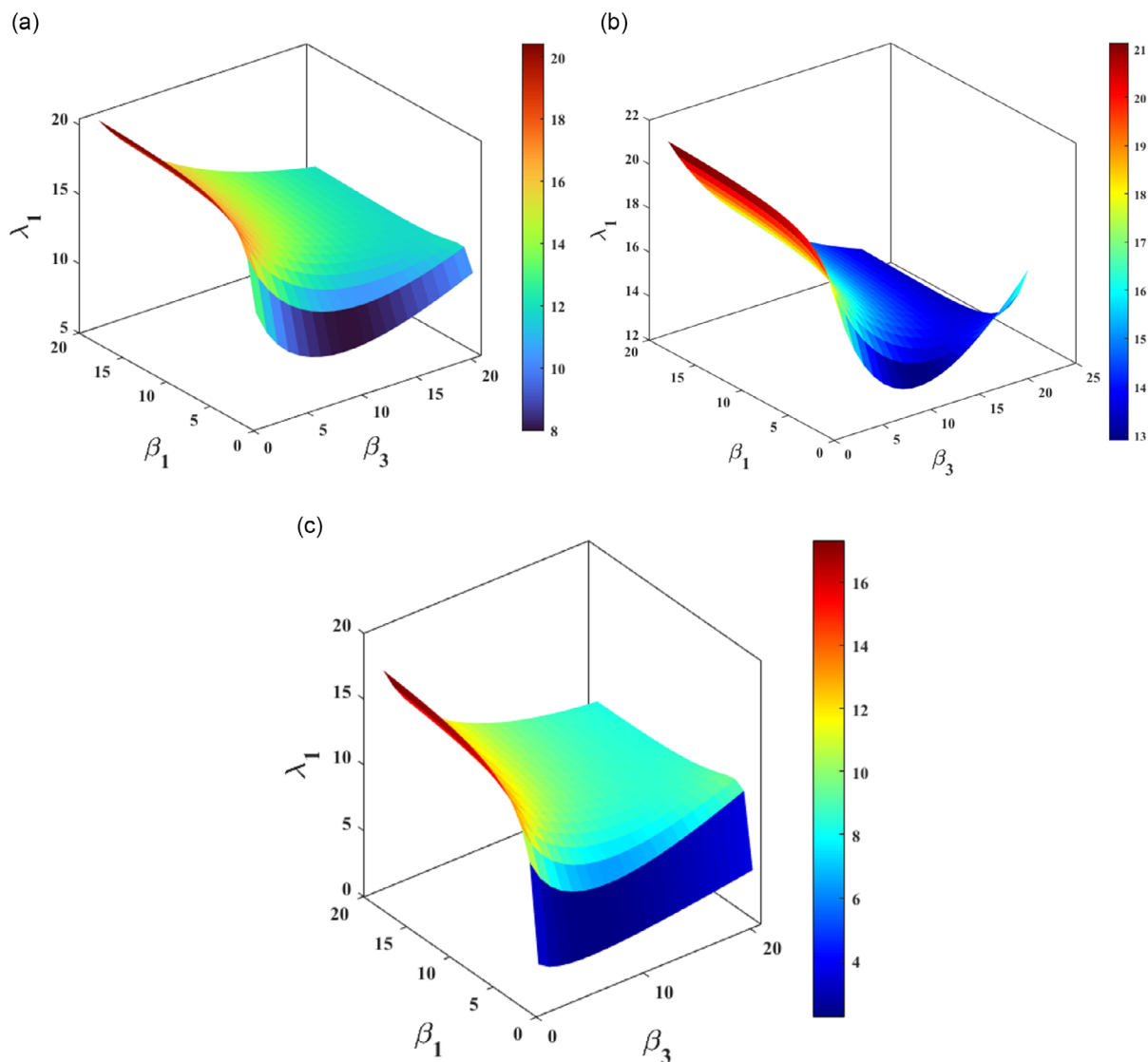


Figure 17. Comparison of dimensionless frequencies λ_1 of the auxetic core nano plate depending on the β_1 and β_3 parameters considering $Br = 0.5$, $Co = 0.5$, $NLTR \Delta T = 0$. The auxetic core material of the smart nanoplate has been determined to be nickel. The core nano plate parameters as considered $a = 1e-6$, $dd = a/100$, $tt = a/500$, $ll = a/100$. a) $Br = 0.5$, $Co = 0.5$, $\theta = 45^\circ$; b) $Br = 0.5$, $Co = 0.5$, $\theta = 15^\circ$; c) $Br = 0.5$, $Co = 0.5$, $\theta = 75^\circ$.

Figure 17 shows the change of dimensionless first frequency of the auxetic core sandwich smart nanoplate according to parameters β_1 and β_3 considering $\theta = 45^\circ$ in Figure 17a, $\theta = 15^\circ$ in Figure 17b, and $\theta = 75^\circ$ in Figure 17c. The parameters β_1 and β_3 have been determined in the range of [1 and 10] with the increment step 0.5. The smart nanoplate's auxetic core is made of nickel, and face plates are made of barium (Br) and cobalt ferrite (Co). The cobalt material compound of the face plate has been defined with $Co = 0.5$ and $Br = 0.5$. The fundamental properties of the nanoplate can be described as follows: $a = 1e-6$, $b = a$, $hh = a/25$, $h_c = hh/5$, $h_r = hh/10$, $h_p = 0.35 \times hh$, $dd = a/100$, $tt = a/500$, $ll = a/100$. As shown in the figures, generally, as the parameter β_1 , the dimensionless first frequency increases even though increasing parameter β_3 decreases in the dimensionless first frequency of the plate.

4. Conclusion

Ultimately, this study has focused on examining the mechanical characteristics of a sandwich nanoplate with an auxetic core, providing light on the behavior of these intelligent materials in different circumstances. The investigation covered various parameters, including the impact of different β_1 values, inclined angles (θ), and material compositions on mechanical properties such as elasticity modulus, shear modulus, tensile modulus, Poisson's ratio, thermal expansion coefficient, and dimensional frequency. The results indicated substantial connections between the examined parameters and the mechanical properties of the intelligent nanoplate. Initially, it was noted that a rise in the β_1 parameter typically resulted in an improvement in the mechanical characteristics of the nanoplate, including the elasticity

modulus in the xx direction (E_{11}^c), shear modulus in the xy plane (G_{12}^c), and tensile modulus in the yz plane (G_{13}^c). This implies that adjusting the aspect ratio of the core components can be a successful approach in customizing the mechanical behavior of auxetic materials. E_{11}^c

Moreover, the impact of inclined angles (θ) on mechanical properties was clarified. However, alterations in θ led to fluctuations in mechanical parameters, with distinct patterns depending on the particular property being analyzed. An increase in θ generally caused a decrease in the elastic modulus in the yy direction (E_c^{22}), shear modulus in the yz plane (G_{23}^c), and thermal expansion coefficient in the xx direction (α_{11}^c). However, it had a positive effect on the Poisson's ratio in both the $x\gamma$ (ν_{12}^c), and γx (ν_{21}^c) directions.

Additionally, the study investigated how the mechanical properties of the smart nanoplate are affected by factors such as the materials used for the face plate and external influences like temperature, magnetic fields, and electric potentials. The investigation revealed that modifying these factors could greatly impact mechanical characteristics, suggesting the possibility of utilizing these intelligent materials for diverse engineering applications. The discoveries have significant engineering consequences. Due to their distinctive mechanical characteristics, auxetic materials exhibit great potential in diverse engineering disciplines, such as aerospace, automotive, biomedical, and structural engineering. Manipulating parameters allows for the customization of mechanical reactions, enabling the design of sophisticated materials with specific functionality, such as enhanced impact resistance, vibration damping, and shape memory capabilities.

In the future, researchers could prioritize various features to advance our comprehension and utilization of auxetic materials. First, researching intricate geometries and material compositions could yield a profound understanding of intelligent nanoplates' behavior under various loading circumstances. Moreover, studying the dynamic behavior of these materials, specifically in reaction to sudden stimuli like impact and vibration, could provide useful insights for practical applications. In addition, the combination of computational modeling and experimental validation can improve the precision and dependability of predictions, making it easier to create strong design recommendations for engineering applications. Furthermore, investigating innovative production methods and addressing scaling concerns could expedite the integration of these materials from experimental studies to viable engineering applications. This study emphasizes the importance of auxetic materials in engineering applications and showcases the possibility of adjusting mechanical properties by manipulating parameters. Utilizing these observations, engineers can facilitate the creation of novel materials and structures with improved performance and functionality, leading to improvements in diverse engineering fields.

This study offers a new perspective on how to customize the mechanical properties of auxetic nanoplates. It shows that by adjusting the β_1 parameter and inclined angles (θ), it is possible to have a considerable impact on the material's elasticity, shear modulus, and Poisson's ratio. This study emphasizes the possibility of enhancing auxetic materials for specific engineering applications by manipulating these characteristics, thereby enabling the development of innovative material designs with

improved impact resistance, vibration damping, and adaptive capabilities in different engineering domains.

Appendix

$$\begin{aligned}
 A_{ij}^{(n)} &= \int_{h_1}^{h_2} C_{ij}^f \{1, z, z^2\} dz + \int_{h_2}^{h_3} C_{ij}^r \{1, z, z^2\} dz \\
 &+ \int_{h_3}^{h_4} C_{ij}^c \{1, z, z^2\} dz + \int_{h_4}^{h_5} C_{ij}^s \{1, z, z^2\} dz \\
 &+ \int_{h_5}^{h_6} C_{ij}^f \{1, z, z^2\} dz \quad n = 0, 1, 2 \\
 \bar{A}_{ij}^{(\bar{n})} &= \int_{h_1}^{h_2} C_{ij}^f f(z) \{1, z, f(z)\} dz + \int_{h_2}^{h_3} C_{ij}^r f(z) \{1, z, f(z)\} dz \\
 &+ \int_{h_3}^{h_4} C_{ij}^c f(z) \{1, z, f(z)\} dz + \int_{h_4}^{h_5} C_{ij}^s f(z) \{1, z, f(z)\} dz \\
 &+ \int_{h_5}^{h_6} C_{ij}^f f(z) \{1, z, f(z)\} dz, \quad \bar{n} = 0, 1, f \\
 \tilde{A}_{ij}^{(\tilde{n})} &= \int_{h_1}^{h_2} C_{ij}^s g'(z) \{1, z, g'(z), f(z)\} dz \\
 &+ \int_{h_2}^{h_3} C_{ij}^c g'(z) \{1, z, g'(z), f(z)\} dz \\
 &+ \int_{h_3}^{h_4} C_{ij}^s g'(z) \{1, z, g'(z), f(z)\} dz \\
 &+ \int_{h_4}^{h_5} C_{ij}^s g'(z) \{1, z, g'(z), f(z)\} dz \\
 &+ \int_{h_5}^{h_6} C_{ij}^s g'(z) \{1, z, g'(z), f(z)\} dz, \quad \tilde{n} = 0, 1, g', f \\
 \tilde{\tilde{A}}_{ij}^{(\tilde{\tilde{n}})} &= \int_{h_1}^{h_2} C_{ij}^s g^2(z) dz + \int_{h_2}^{h_3} C_{ij}^c g^2(z) dz + \int_{h_3}^{h_4} C_{ij}^s g^2(z) dz \\
 &+ \int_{h_4}^{h_5} C_{ij}^s g^2(z) dz + \int_{h_5}^{h_6} C_{ij}^s g^2(z) dz
 \end{aligned} \tag{A1}$$

$$\begin{aligned}
 B_{e_{ij}}^{(k)} &= - \left[\int_{h_1}^{h_2} e_{ij} \left(\frac{2\varphi_0}{h_s} \right) \left\{ z, f(z), g'(z), \left(\frac{h_s}{2\varphi_0} \right) \cos \left(\frac{\pi z_2}{h_s} \right) \right\} dz \right. \\
 &+ \left. \int_{h_5}^{h_6} e_{ij} \left(\frac{2\varphi_0}{h} \right) \left\{ z, f(z), g'(z), \left(\frac{h_s}{2\varphi_0} \right) \cos \left(\frac{\pi z}{h_s} \right) \right\} dz \right], \\
 &k = 1, f, g', g \\
 \bar{B}_{e_{ij}}^{(k)} &= - \left[\int_{h_1}^{h_2} e_{ij} \left[\frac{\pi}{h_s} \sin \left(\frac{\pi z_1}{h_s} \right) \right] \{1, z, f(z), g'(z)\} dz \right. \\
 &+ \left. \int_{h_5}^{h_6} e_{ij} \left[\frac{\pi}{h} \sin \left(\frac{\pi z}{h} \right) \right] \{1, z, f(z), g'(z)\} dz \right], \quad k = 0, 1, f, g' \\
 B_{q_{ij}}^{(k)} &= - \left[\int_{h_1}^{h_2} q_{ij} \left(\frac{2\varphi_0}{h_s} \right) \left\{ z, f(z), g'(z), \left(\frac{h_f}{2\varphi_0} \right) \cos \left(\frac{\pi z_1}{h_s} \right) \right\} dz \right. \\
 &+ \left. \int_{h_5}^{h_6} q_{ij} \left(\frac{2\varphi_0}{h} \right) \left\{ z, f(z), g'(z), \left(\frac{h}{2\varphi_0} \right) \cos \left(\frac{\pi z}{h} \right) \right\} dz \right], \\
 &k = 1, f, g', g \\
 \bar{B}_{q_{ij}}^{(k)} &= - \left[\int_{h_1}^{h_2} q_{ij} \left[\frac{\pi}{h_s} \sin \left(\frac{\pi z_1}{h_s} \right) \right] \{1, z, f(z), g'(z)\} dz \right. \\
 &+ \left. \int_{h_5}^{h_6} q_{ij} \left[\frac{\pi}{h} \sin \left(\frac{\pi z}{h} \right) \right] \{1, z, f(z), g'(z)\} dz \right], \quad k = 0, 1, f, g'
 \end{aligned} \tag{A2}$$

$$P_{\varepsilon_{ij}}^{(n)} = - \left[\int_{h_1}^{h_2} \varepsilon_{ij} \left\{ \left(\frac{2\varphi_0}{h_s} \right) \left[\frac{\pi}{h_s} \sin \left(\frac{\pi z_1}{h_s} \right) \right], \left[\frac{\pi}{h_s} \sin \left(\frac{\pi z_1}{h_s} \right) \right]^2, \left[\cos \left(\frac{\pi z_1}{h_s} \right) \right]^2 \right\} dz + \int_{h_5}^{h_6} \varepsilon_{ij} \left\{ \left(\frac{2\varphi_0}{h} \right) \left[\frac{\pi}{h} \sin \left(\frac{\pi z}{h} \right) \right], \left[\frac{\pi}{h} \sin \left(\frac{\pi z}{h} \right) \right]^2, \left[\cos \left(\frac{\pi z}{h} \right) \right]^2 \right\} dz \right],$$

$$n = 1, s2, c2$$

$$P_{g_{ij}}^{(n)} = - \left[\int_{h_1}^{h_2} g_{ij} \left\{ \left(\frac{2\varphi_0}{h_s} \right) \left[\frac{\pi}{h_s} \sin \left(\frac{\pi z_1}{h_s} \right) \right], \left[\frac{\pi}{h_s} \sin \left(\frac{\pi z_1}{h_s} \right) \right]^2, \left[\cos \left(\frac{\pi z_1}{h_s} \right) \right]^2 \right\} dz + \int_{h_5}^{h_6} g_{ij} \left\{ \left(\frac{2\varphi_0}{h} \right) \left[\frac{\pi}{h} \sin \left(\frac{\pi z}{h} \right) \right], \left[\frac{\pi}{h} \sin \left(\frac{\pi z}{h} \right) \right]^2, \left[\cos \left(\frac{\pi z}{h} \right) \right]^2 \right\} dz \right],$$

$$n = 1, s2, c2$$

$$P_{\mu_{ij}}^{(n)} = - \left[\int_{h_1}^{h_2} \mu_{ij} \left\{ \left(\frac{2\varphi_0}{h_s} \right) \left[\frac{\pi}{h_s} \sin \left(\frac{\pi z_1}{h_s} \right) \right], \left[\frac{\pi}{h_s} \sin \left(\frac{\pi z_1}{h_s} \right) \right]^2, \left[\cos \left(\frac{\pi z_1}{h_s} \right) \right]^2 \right\} dz + \int_{h_5}^{h_6} \mu_{ij} \left\{ \left(\frac{2\varphi_0}{h} \right) \left[\frac{\pi}{h} \sin \left(\frac{\pi z}{h} \right) \right], \left[\frac{\pi}{h} \sin \left(\frac{\pi z}{h} \right) \right]^2, \left[\cos \left(\frac{\pi z}{h} \right) \right]^2 \right\} dz \right],$$

$$n = 1, s2, c2$$

$$K_{11} = -c_2 \left(\alpha^2 A_{11}^{(0)} + \beta^2 A_{66}^{(0)} \right)$$

$$K_{12} = -c_2 \alpha \beta \left(A_{12}^{(0)} + A_{66}^{(0)} \right)$$

$$K_{13} = c_2 \left(\alpha^3 A_{11}^{(1)} + \alpha \beta^2 \left(A_{12}^{(1)} + 2A_{66}^{(1)} \right) \right)$$

$$K_{14} = c_2 \left(\alpha^3 \bar{A}_{11}^{(0)} + \alpha \beta^2 \left(\bar{A}_{12}^{(0)} + 2\bar{A}_{66}^{(0)} \right) \right)$$

$$K_{15} = c_2 \alpha \bar{A}_{13}^{(0)}$$

$$K_{16} = c_2 \alpha \bar{B}_{e31}^{(0)}$$

$$K_{17} = c_2 \alpha \bar{B}_{q31}^{(0)}$$

$$K_{22} = -c_2 \left(\beta^2 A_{22}^{(0)} + \alpha^2 A_{66}^{(0)} \right)$$

$$K_{23} = -c_2 \left(\beta^3 A_{22}^{(1)} + \beta \alpha^2 \left(A_{12}^{(1)} + 2A_{66}^{(1)} \right) \right)$$

$$K_{24} = c_2 \left(\beta^3 \bar{A}_{22}^{(0)} + \beta \alpha^2 \left(\bar{A}_{12}^{(0)} + 2\bar{A}_{66}^{(0)} \right) \right)$$

$$K_{25} = c_2 \beta \bar{A}_{23}^{(0)}$$

$$K_{26} = c_2 \beta \bar{B}_{e32}^{(0)}$$

$$K_{27} = c_2 \beta \bar{B}_{q32}^{(0)}$$

$$K_{33} = \alpha^2 [1 + \mathcal{B}(\alpha^2 + \beta^2)] (N_0 + p_{e31} + p_{q31}) + \beta^2 [1 + \mathcal{B}(\alpha^2 + \beta^2)] (\gamma N_0 + p_{e32} + p_{q32}) - c_2 \left(\alpha^4 A_{11}^{(2)} - \beta^4 A_{22}^{(2)} - 2\alpha^2 \beta^2 \left(A_{12}^{(2)} + 2A_{66}^{(2)} \right) \right)$$

$$K_{34} = -c_2 \left(\alpha^4 \bar{A}_{11}^{(1)} + \beta^4 \bar{A}_{22}^{(1)} + 2\alpha^2 \beta^2 \left(\bar{A}_{12}^{(1)} + 2\bar{A}_{66}^{(1)} \right) \right)$$

$$K_{35} = -c_2 \left(\alpha^2 \bar{A}_{13}^{(1)} + \beta^2 A_{23}^{(1)} \right)$$

$$K_{36} = -c_2 \left(\alpha^2 \bar{B}_{e31}^{(1)} + \beta^2 \bar{B}_{e32}^{(1)} \right)$$

$$K_{37} = -c_2 \left(\alpha^2 \bar{B}_{q31}^{(1)} + \beta^2 \bar{B}_{q32}^{(1)} \right)$$

$$K_{44} = -c_2 \left(\alpha^2 \hat{A}_{55}^{(0)} + \beta^2 \hat{A}_{44}^{(0)} + \alpha^4 \bar{A}_{11}^{(f)} + \beta^4 \bar{A}_{22}^{(f)} + 2\alpha^2 \beta^2 \left(\bar{A}_{12}^{(f)} + 2\bar{A}_{66}^{(f)} \right) \right)$$

$$K_{45} = -c_2 \left(\alpha^2 \left(\bar{A}_{13}^{(f)} + \hat{A}_{55}^{(0)} \right) + \beta^2 \left(\bar{A}_{23}^{(f)} + \hat{A}_{44}^{(0)} \right) \right)$$

$$K_{46} = c_2 \left(\alpha^2 \left(B_{e15}^{(g)} - \bar{B}_{e31}^{(f)} \right) + \beta^2 \left(B_{e24}^{(g)} - \bar{B}_{e32}^{(f)} \right) \right)$$

$$K_{47} = c_2 \left(\alpha^2 \left(B_{q15}^{(g)} - \bar{B}_{q31}^{(f)} \right) + \beta^2 \left(B_{q24}^{(g)} - \bar{B}_{q32}^{(f)} \right) \right)$$

$$K_{55} = -c_2 \left(\bar{A}_{33}^{(g)} + \alpha^2 \hat{A}_{55}^{(0)} + \beta^2 \hat{A}_{44}^{(0)} \right)$$

$$K_{56} = c_2 \left(\alpha^2 B_{e15}^{(g)} + \beta^2 B_{e24}^{(g)} - \bar{B}_{e33}^{(g)} \right)$$

$$K_{57} = c_2 \left(\alpha^2 B_{q15}^{(g)} + \beta^2 B_{q24}^{(g)} - \bar{B}_{q33}^{(g)} \right)$$

$$K_{66} = c_2 \left(\alpha^2 p_{e11}^{(c2)} + \beta^2 p_{e22}^{(c2)} + p_{e33}^{(s2)} \right)$$

$$K_{66} = c_2 \left(\alpha^2 p_{g11}^{(c2)} + \beta^2 p_{g22}^{(c2)} + p_{g33}^{(s2)} \right)$$

$$K_{77} = c_2 \left(\alpha^2 p_{\mu 11}^{(c2)} + \beta^2 p_{\mu 22}^{(c2)} + p_{\mu 33}^{(s2)} \right)$$

$$c_2 = (1 + l_m (\alpha^2 + \beta^2))$$

$$(A3) \quad M_{11} = -[1 + \mathcal{B}(\alpha^2 + \beta^2)] m_0$$

$$M_{13} = \alpha [1 + \mathcal{B}(\alpha^2 + \beta^2)] m_1$$

$$M_{14} = \alpha [1 + \mathcal{B}(\alpha^2 + \beta^2)] m_3$$

$$M_{12} = M_{15} = M_{16} = M_{17} = 0$$

$$M_{22} = -[1 + \mathcal{B}(\alpha^2 + \beta^2)] m_0$$

$$M_{23} = \beta [1 + \mathcal{B}(\alpha^2 + \beta^2)] m_1$$

$$M_{24} = \beta [1 + \mathcal{B}(\alpha^2 + \beta^2)] m_3$$

$$M_{25} = M_{26} = M_{27} = 0$$

$$M_{33} = -[1 + \mathcal{B}(\alpha^2 + \beta^2)] m_0 - (\alpha^2 + \beta^2) [1 + \mathcal{B}(\alpha^2 + \beta^2)] m_2$$

$$M_{34} = -[1 + \mathcal{B}(\alpha^2 + \beta^2)] m_0 - (\alpha^2 + \beta^2) [1 + \mathcal{B}(\alpha^2 + \beta^2)] m_4$$

$$M_{35} = -[1 + \mathcal{B}(\alpha^2 + \beta^2)] m_6$$

$$M_{36} = M_{37} = 0$$

$$M_{44} = -[1 + \mathcal{B}(\alpha^2 + \beta^2)] m_0 - (\alpha^2 + \beta^2) [1 + \mathcal{B}(\alpha^2 + \beta^2)] m_5$$

$$M_{45} = -[1 + \mathcal{B}(\alpha^2 + \beta^2)] m_6$$

$$M_{55} = -[1 + \mathcal{B}(\alpha^2 + \beta^2)] m_7$$

$$M_{56} = M_{57} = M_{66} = M_{67} = M_{77} = 0$$

Conflict of Interest

The authors declare no conflict of interest.

Data Availability Statement

The data that support the findings of this study are available from the corresponding author upon reasonable request.

Keywords

auxetic cores, auxetic materials, magneto-electroelastic, sandwich plates, smart nanoplates

Received: April 1, 2024

Revised: May 21, 2024

Published online:

- [1] D. Atilla Yolcu, B. Okutan Baba, *Compos. Struct.* **2024**, 329, 117749.
- [2] H. Lu, X. Wang, T. Chen, *Thin-Walled Struct.* **2023**, 191, 111011.
- [3] D. Cao, *Prog. Addit. Manuf.* **2023**, <https://doi.org/10.1007/s40964-023-00508-6>.
- [4] H. M. Öztemiz, Ş. Temiz, *Int. J. Solids Struct.* **2024**, 286–287, 112546.
- [5] A. Moradi, R. Ansari, M. K. Hassanzadeh-Aghdam, S.-H. Jang, *Eur. J. Mech. A. Solids* **2024**, 103, 105182.
- [6] G. Di Cara, M. D'Ottavio, O. Polit, *Compos. Struct.* **2024**, 330, 117856.
- [7] S. Chakraborty, T. Dey, *Eur. J. Mech. A. Solids* **2023**, 98, 104894.
- [8] P. Singh, J. Sheikh, B. K. Behera, *Thin-Walled Struct.* **2024**, 195, 111376.
- [9] K. J. Kontoleon, K. Georgiadis-Filikas, K. G. Tsikaloudaki, T. G. Theodosiou, C. S. Giarma, C. G. Papanicolaou, T. C. Triantafyllou, E. K. Asimakopoulou, *J. Build. Eng.* **2022**, 52, 104479.
- [10] H. Zniker, I. Feddal, B. Ouaki, S. Bouzakraoui, *J. Fail. Anal. Prev.* **2023**, 23, 66.
- [11] D. J. Sypeck, *Appl. Compos. Mater.* **2005**, 12, 229.
- [12] V. Birman, G. A. Kardomateas, *Composites, Part B* **2018**, 142, 221.
- [13] M. Karimiasl, A. Alibeigloo, *Commun. Nonlinear Sci. Numer. Simul.* **2023**, 123, 107267.
- [14] P. Q. Li, K. F. Wang, B. L. Wang, *Thin-Walled Struct.* **2024**, 196, 111479.
- [15] M. Karimiasl, A. Alibeigloo, *Microsyst. Technol.* **2023**, 29, 1739.
- [16] M. Zanjanchi, M. Ghadiri, S. Sabouri-Ghomi, *Eur. J. Mech. A. Solids* **2023**, 102, 105109.
- [17] H.-Q. Tran, V.-T. Vu, V.-L. Nguyen, M.-T. Tran, *Thin-Walled Struct.* **2023**, 191, 111141.
- [18] X. Huang, J. Yang, X. Wang, I. Azim, *Eng. Comput.* **2022**, 38, 55.
- [19] X. Liu, Y. Li, H. Hu, Z. Zhang, *Mater. Sci. Eng., A.* **2023**, 830, 142210.
- [20] J. Chen, L. Wang, H. Wang, *Composites, Part B* **2024**, 247, 110269.
- [21] Y. Zhou, P. Li, Z. Xie, *Smart Mater. Struct.* **2023**, 33, 25001.
- [22] V. D. Quang, T. Q. Quan, P. Tran, *Thin-Walled Struct.* **2022**, 173, 108935.
- [23] G. Y. Zhang, Y. L. Qu, X.-L. Gao, F. Jin, *Mech. Mater.* **2020**, 149, 103412.
- [24] K. K. Żur, M. Arefi, J. Kim, J. N. Reddy, *Composites, Part B* **2020**, 182, 107601.
- [25] Z. Lyu, M. Ma, *Thin-Walled Struct.* **2023**, 191, 111004.
- [26] L.-L. Gan, G.-L. She, *Acta Astronaut.* **2024**, 214, 11.
- [27] Y. Zheng, Y. Zhou, F. Wang, C. Chen, *Eur. J. Mech. A. Solids* **2024**, 103, 105158.
- [28] K. Chadha, V. Mahesh, A. S. Mangalasseri, V. Mahesh, *Thin-Walled Struct.* **2023**, 184, 110533.
- [29] F. Pehlivan, I. Esen, K. G. Aktas, *Mech. Adv. Mater. Struct.* n.d, 1, <https://doi.org/10.1080/15376494.2024.2303377>.
- [30] M. A. Koç, İ. Esen, M. Eroğlu, *Mech. Adv. Mater. Struct.* **2023**, <https://doi.org/10.1080/15376494.2023.2199412>.
- [31] M. Eroğlu, İ. Esen, M. A. Koç, *Acta Mech.* **2024**, 235, 2415.
- [32] M. Eroğlu, İ. Esen, M. A. Koç, *Mech. Based Des. Struct. Mach.* n.d, 1, <https://doi.org/10.1080/15397734.2024.2308659>.
- [33] P. Van Lieu, A. M. Zenkour, G. T. Luu, *Eur. J. Mech. A. Solids* **2024**, 103, 105181.
- [34] V. D. Nguyen, Q. V. Vu, *Alexandria Eng. J.* **2023**, 69, 135.
- [35] M. Sarafraz, H. Seidi, F. Kakavand, N. S. Viliiani, *Thin-Walled Struct.* **2023**, 183, 110331.
- [36] Y. S. Touloukian, *Thermophysical Properties of High Temperature Solid Materials*, Volume 4. Oxides And Their Solutions And Mixtures. Part 1, Vol. 1, Macmillan, New York, NY **1967**.
- [37] Y. S. Touloukian, *Thermophysical Properties of High Temperature Solid Materials*, Volume 4. Oxides And Their Solutions And Mixtures. Part 1, Vol. 1, Macmillan, New York **1966**.
- [38] F. Li, W. Yuan, C. Zhang, *J. Sandwich Struct. Mater.* **2021**, 24, 565.
- [39] Y. Kiani, M. R. Eslami, *Composites, Part B* **2013**, 45, 101.
- [40] D. G. Zhang, *Meccanica* **2014**, 49, 283.
- [41] A. C. Eringen, *Int. J. Eng. Sci.* **1983**, 21, 741.
- [42] C. W. Lim, G. Zhang, J. N. Reddy, *J. Mech. Phys. Solids* **2015**, 78, 298.
- [43] L. Li, X. Li, Y. Hu, *Int. J. Eng. Sci.* **2016**, 102, 77.
- [44] A. Farajpour, A. Rastgoo, *Results Phys.* **2017**, 7, 1367.
- [45] A. C. Eringen, *J. Appl. Phys.* **1983**, 54, 4703.
- [46] E. Pan, P. R. Heyliger, *J. Sound Vib.* **2002**, 252, 429.
- [47] M. Arefi, A. M. Zenkour, *J. Sandwich Struct. Mater.* **2016**, 18, <https://doi.org/10.1177/1099636216652581>.
- [48] M. Arefi, A. M. Zenkour, *Steel Compos. Struct.* **2018**, 26, 421.
- [49] J. N. Reddy, in *Theory and Analysis of Elastic Plates and Shells* **2020**, <https://doi.org/10.1201/9780849384165-6>.
- [50] G. T. Monaco, N. Fantuzzi, F. Fabbrocino, R. Luciano, *Nanomaterials.* **2021**, 11, 1.
- [51] F. Ramirez, P. R. Heyliger, E. Pan, *Mech. Adv. Mater. Struct.* **2006**, 13, <https://doi.org/10.1080/15376490600582750>.
- [52] R. Aghababaei, J. N. Reddy, *J. Sound Vib.* **2009**, 326, 277.
- [53] J. N. Reddy, C. D. Chin, *J. Therm. Stresses* **1998**, 21, 593.